A Thin-Film of Mechanochemically Synthesized Nanoparticles:

An experimental and theoretical exploration of an absorber compound for photovoltaic devices

by

Victor Bradley Bednar

BSc., Eastern Oregon University, 2010

A THESIS SUBMITTED IN PARTIAL FULFILLMENT OF
THE REQUIREMENTS FOR THE DEGREE OF

MASTER OF APPLIED SCIENCE

in

The Faculty of Graduate and Postdoctoral Studies
(Electrical and Computer Engineering)

THE UNIVERSITY OF BRITISH COLUMBIA
(Vancouver)

April 2017

Abstract

Nearly 200 years after the discovery of the photovoltaic effect, harvesting energy from the sun is finally becoming a price competitive marketing option for power generation. Government and private investments, motivated by a social awareness of environmental issues cause by prominent power generation methods, have helped create this opportunity to advance earth conscientious, green energy solutions. As inorganic nanoparticles in solar cell layers are one of the forefront areas of interest for solar cell research, mechanochemical material synthesis has been used for a scalable production of Fe_2GeS_4 nanoparticles carried out via ball milling. The compound is composed of earth-abundant materials, and ball milling allows for a solution free process, which minimizes chemical waste from material synthesis. The viability of this promising compound has been previously mentioned and herein confirmed. X-Ray Powder Diffraction (XRD) showed a successful synthesis, and optical characterization confirmed favorable absorption properties for solar cell implementation. New methods were implemented in doping the nanoparticles, which lead to an observable photovoltaic response from a simple prototype architecture implementing the Fe_2GeS_4 nanoparticles. The thin film deposition of the nanoparticles used for prototype implementation should allow for cost effective and scalable manufacturing.

Since ball milling is also cost effective and scalable, an empirical model implementing probabilistic logic is developed and shown as capable to fit experimental data via measurable parameters. The eventual optimization possibilities for minimizing manufacturing costs, as well as enhancement of general scientific

understanding for an underrepresented branch of theory, mechanochemical solid state reactions, motivated this work. Modeling of Fe_2GeS_4 production, as a solid state chemical reaction, demonstrates a proof of principle application. Potential applications are not limited to mechanochemical synthesis. Extensions to other reaction types are possible as the model utilizes chemical kinetics theory in a generalized fashion. The demonstration focuses on a sigmoid trend, as observed in Fe_2GeS_4 synthesis, though other profiles are attainable.

Lay Summary

Rising concerns about sustaining the earth and meeting the energy demands of society both have led to great progress in using the sun to generate electricity. In this work, earth abundant resources are used to build a prototype solar cell for harvesting the sun's energy to generate electricity. Though these materials have previously been investigated, new options have been realized in this research by investigating methods not used previously with these materials.

To complement this production, with an opportunity to one day improve the manufacturing costs of such a solar cell, a mathematical model was developed. The model introduces a new approach to enhance the understanding of the mechanical means used to create novel compounds. Both the mathematical model and the techniques used in making a prototype show usable results with promise for future implementations.

Preface

All text within this document, unless quoted, have been written by the author. In Chapter 3, the model was developed in full by the author. The code used to run simulations, seen in Appendix A.1 was written by the author, with the exception of the "RK4 Loop" which has been repurposed and edited by the author with the permission of the original author, Anthony A. Tovar. The code was run on a computer built by the author. The experimental and analytical works presented in Chapters 4 and 5 were done by the author. Development of the research goals and experiments contained in this thesis were thought up by the author and implemented under the guidance and approval of Dr. Peyman Servati.

Table of Contents

List of Tables

List of Figures

List of Graphs

Glossary

SEM	Scanning Electron Microscopy
XRD	X-Ray Powder Diffraction
EDX	Energy-dispersive X-ray
ITO	Indium Tin Oxide
SMU	Source Measure Unit

Acknowledgments

I am very grateful to Rowshan Rahmanian, Zenan Jiang, and Yan Wang for kindly answering questions, helping with equipment training, and for their general good company around the lab and office along with all other members of the Flexible Electronics and Energy Lab group. Pursuit of this research would not have been possible without the use of equipment within the Advanced Fibrous Materials, Advanced Materials and Process Engineering Laboratory. Anita Lam, your passion for X-ray diffraction made it easy to learn. Dr. Frank Ko, your literary insights were greatly appreciated. Thank you, Dr. Peyman Servati for providing this opportunity, an inquisitive environment, and financial support for my endeavors.

The University of British Columbia Dance Club and others in the ballroom dance community, what a great assortment of people who listen well to each other's work with intense sincerity (a wonderful, happy bunch of dancing scientist, students, and community members).

To my family, I appreciate your endless understanding with everything I choose to pursue in life.

Dedication

To I Am, beside me always – –my eternal gratitude.

Chapter 1

Introduction

> *Seemeth it a small thing unto you to have eaten up the good pasture,*
> *but ye must tread down with your feet the residue of your pastures?*
> *and to have drunk of the deep waters, but ye must foul the residue*
> *with your feet?* — Ezekiel 34:18 [1]

Since early times, we have known that our existence did not come without an impact to the very land that we rely on for our survival. Currently, our energy demands immensely impact our environment. In order to bring about a cessation to our energy related issues, better green energy solutions are necessary. Can we resolve these issues with solar energy harvesting? Hopefully, the explanations in this chapter will make the possibilities clear. With an understanding of the available solutions and methods used in these works, in Chapter 2, we move forward to more specifics on why we pursue this research path and what has been done previously. The focused goal of this research is to test the viability of mechanochemically synthesized nanoparticles in photovoltaic devices–specifically Fe_2GeS_4.

1.1 Light

One can hardly discuss solar energy harvest without a light grasp on photons. Often things of intangible form leave those studying the phenomena of nature in awe. Light is of this category, and we owe our sight to such an existence. However, understanding its mysteries has been an undertaking for centuries which continues to this day.

Christiaan Huygens was the first to write on the wave properties of light. Sir Isaac Newton, in juxtaposition to this view, advanced optics and wrote on the corpuscular nature of light. Thomas Young confirmed light as a transverse wave; however, it can cross the void transmitting energy in the absence of any medium. This becomes the first important piece of the puzzling experience for one dedicated to sunlight energy harvesting via solar cells. Wave properties of light can be understood using mathematical theories brought together by James Clerk Maxwell and made more usable by Oliver Heaviside.

The quantity of energy can be understood through the corpuscular property of light. These theories were advanced by Max Planck and Albert Einstein. This quantization becomes the second important piece of information for light energy harvesting. For a more in-depth look into the history of light, and those who have made discoveries with a lasting impact, various physics history books for undergraduates gather such material. For example, Kuehn [2] and Shamos [3] do just that in their books.

When a photon interacts with matter, there are various options. For solar energy harvesting applications, we will focus on the interactions of photons with materials and how it effects electrons. For starters, the photovoltaic effect.

1.2 Photovoltaics

The photovoltaic effect is the process through which a potential is observed, across the terminals of a cell, as a result of a photon's interacting with the material. Taking advantage of different designs, which focus on the various aspects of a solar cell, should at a minimum result in a photopotential observation. So what are the various phenomena which allow for such an observation?

First, a photon has to be absorbed by a material. Though there are other ways to draw signal from light, for example, read on some ways of how to detect an evanescent wave [4, 5]; however, we will focus on the main processes in a photovoltaic. Ignoring how or why (unless one wants to study optics and quantum field theory), think that the energy of a photon is completely transferred to an electron during absorption, and the photon is then no more. Let us start with a simplified idea such as an atom with one proton and one electron. In the case of this individual atom, the energy can increase the electrical potential between the electron and the nucleus of the atom. Videlicet, the spatial distance between the two electrically attracted particles increases. If the photon carries enough energy, the electron can become free of the nucleus (ionization). This is a simplified view of the photoelectric effect described by Albert Einstein–electrons freed from material by the properly corresponding light energy packets (photons). In bulk material, this energy has some other properties as well. For example, the light might penetrate some distance into the material before it is absorbed, and then the electron might not be able to have enough energy to propagate that distance and leave the material. However, the main idea here is that material needs to absorb light and "free" electrons from their bound states.

How we use these electrons is another important aspect for observing a photopotential. For example, in semiconducting materials, electrons spatially restricted by the material bonds are not free to move around enough to play a major role in electrical conduction. The "free" electrons do have enough energy. Thus, this energy difference between bound (valence band electrons) and "free" (conduction band electrons) electrons forms a gap between band energies. If a photon has enough energy to free a bound electron from a state in the valence band to a state in the conduction band, a physical distance between the location where the electron was bound and its new "free" location is observed. This pair (a "free" electron and its bound location) are referred to as an electron-hole pair. the electrical potential between the pair will match that of the band gap energy between the valence and conduction bands. That is to say, even if a photon imparts more energy on an electron, that energy will dissipate into the system (heat, photon emissions, vibrations, etc.). Thus, the observed photopotential depends on the band gap of materials involved in absorbing photons.

Nothing says these spatially separated charged structures maintain their potential indefinitely. Quite the opposite is often the observed case. The electrons simply recombine with their hole or the hole from another “free” electron. Thus, the terms carrier generation, carrier recombination, and carrier lifetime are used for describing the aforementioned phenomena. Carrier generation is a measure of electron-hole pair production. Carrier recombination is a measure of the pair recombining such that a conduction band electron returns to its bound valence band state. Carrier lifetime is a measurement regarding the time between carrier generation and carrier recombination for an electron-hole pair. For over one hundred years, we have endeavored to optimize cells by designing architectures that put the photovoltaic effect to use in the harvesting of solar radiation energy.

Becquerel [6] writes the first account of the photovoltaic effect in 1839. His experiments used a setup that would now fall in the photoelectrochemical cell category. Adams and Day [7] later (1877) demonstrate a solid-state setup. Finally, the current industry leader makes a partial debut, in 1946, when Ohl [8] patents a light sensitive device made with silicon. This idea becomes a start for the first success story in the solar cell industry when Chapin et al. [9] make a six percent efficient silicon solar cell in 1954. Today, research continues to invest efforts to continue this story until solar cells are realized for their unequivocal superiority in energy production.

1.2.1 Architectural Variations

The United States Department of Energy [10] categorizes photovoltaics based on various elements and their laboratory, the National Renewable Energy Laboratory [11], places those into the following categories: high-efficiency crystalline, polycrystalline thin films, and emerging technologies. The current research efficiencies of these various types can be viewed in Figure 1.1

For starters, let us look at the advantages and disadvantages of the various architectures in the categories outlined by the National Renewable Energy Laboratory [11].

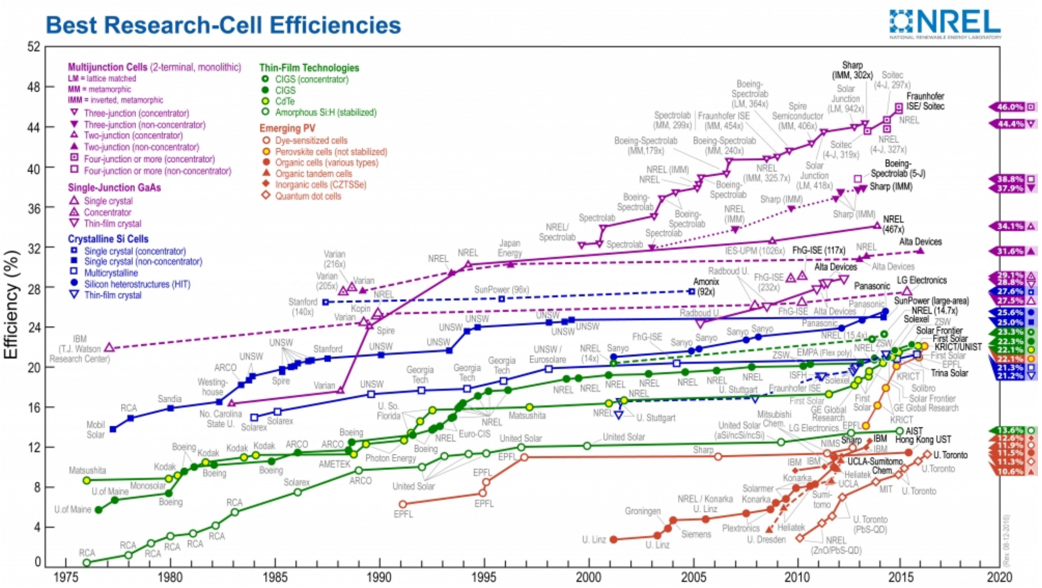

Figure 1.1: Solar Cell efficiencies as listed by the National Renewable Energy Laboratory [12].

High-Efficiency Crystalline Solar Cells

From Figure 1.1, it can be seen that crystalline cells lead in efficiency–especially multijunction cells. So, what are some of the pitfalls? Cost is an obvious boundary. That is to say, though they lead in industry due to years of research and manufacturing investments, we near the limits of what can be accomplished by such means without yet meeting our competitive market goals to overtake other energy sources.

Why are crystalline solar cells the most efficient? One reason has to do with the discontinuities in materials that are not crystalline. As mentioned in Section 1.2, carrier generation, recombination, and lifetime are all important in photovoltaics. Discontinuities of a material's (not perfectly crystalline) structure lead to sinks and sources for electrons within the material. By discontinuity, I mean to express any disruption to a perfect lattice structure. These arise as distortions in the lattice, to name a few: due to physical strains and stresses; chemical impurities causing lattice distortions; and breaks in bonds from fractures, cleavages, and material growth edges. Therefore, carrier lifetime decreases while recombination and possibly generation via non-photon-induced means increases. All of these lead to a decrease in utilizing photons to generated power for external connections on a solar cell. In order to successfully extract a current from a photovoltaic device, one electrode needs to supply electrons for a current and the other needs to accept electrons (or supply holes if one likes to think of holes as carriers). Thus, pair production with long lifetimes is desirable. Since discontinuities sequester our pairs and inhibit our photo production, keeping the material as pure and crystalline as possible is desirable.

This leads to a few of the downfalls of crystalline solar cells. Since a continuous crystal structure is desirable, material boundaries, an absorber/electrode boundary for example, lead to the same issues as discontinuities within a single material. Thus, recombination, and such, at material surfaces becomes a large issue that has been a target in improving crystalline solar cell performance. Another issue is the cost of simply producing highly crystalline materials. Whether growing monocrystalline Silicon via the Czochralski process or layering a multijunction cell via epitaxial growth, most methods for obtaining these extremely pure and highly crystalline materials are expensive.

Finally, as these are crystalline, brittleness becomes a mechanical pitfall for these types of solar cells. Much has been done to improve the ruggedness of solar cells. This and flexibility are partial reasons for the development of other architectures along with cost and market variety to shift the monopolistic competition toward that of a competitive market–so as to drive down the cost of energy.

Polycrystalline Thin Film Solar Cells

As previously mentioned, typical crystalline solar cells are brittle, and this lack of ruggedness and flexibility can hinder popularity for the same reason as to why plastic is often more popular than glass. Polycrystalline thin film solar cells address this issue and some others.

Though Silicon is one of the most abundant earth crust elements, as previously mentioned, crystalline and pure absorbers made from Silicon are expensive. Thin cells, comparatively, use less material and can be made quickly and inexpensively. As can be seen in Figure 1.1, polycrystalline thin film cells have reached over 20% efficiencies in laboratory environments. Though this only comes close to the bottom level efficiencies as seen in crystalline solar cells, such as a single crystal Silicon solar cell without a sunlight concentrator, there is the large benefit of cheaper manufacturing. Therefore, the second largest market share in the solar cell industry is held by polycrystalline solar cells.

So, as the cheaper and fairly efficient alternative, why are polycrystalline thin film solar cells not dominating the market? Well, they are still not as efficient, and their commercial counterparts suffer a larger disparity between their laboratory performance and their commercial performance when compared to the crystalline Silicon technologies. This is partially due to a number of years of research and investment into Silicon technologies, to which polycrystalline thin film technologies are behind many years in industrial investment and a fair amount behind in research interests as well. This also leaves the question of the stability of these solar cells, as they do not have the proven reliability of crystalline Silicon solar cells. Finally, earth abundance and safety are hindrances to these types of solar cells making a large market impact. Some of the more dominate architectures, Cadmium Telluride thin cells, for example, use both rare and toxic materials.

Emerging Technologies for Solar Cells

Moving forward, current research tries to correct the shortcomings of both of the aforementioned (crystalline and polycrystalline) solar cell technologies. Thus, aims are often directed toward addressing some or all of the concerns: namely, environmental factors, stability, cost, and efficiency all can play a role in the material selection and implementation methods. It may be best to break emerging technologies into categories similar to those seen in Figure 1.1. These include organic, inorganic, and hybrid solar cells.

Organic solar cells, by the very nature of their name, include carbon compounds. These molecules are slightly different in electron sharing. As a comparison with to the band states used to discuss electron levels in semiconductors, instead of valence and conduction band states for electrons to occupy, there are the lowest unoccupied molecular orbital and highest occupied molecular orbital respectively. Though the mechanisms are different, carrier pairs and mobility of those carriers to power external devices are still necessary. Some of the benefits include low production cost, various absorption spectrum selection, and possibly use with flexible substrates. The efficiency and stability of these types of cells are still lacking too much. Thus, a large market impact has yet to be made.

Inorganic solar cells have already made their impact. Silicon leads the industry and other leading solar cells are also made using typical semiconductor materials. advancement in the section of the industry works to capitalize every bit possible on current technologies; however, as theoretical efficiency limits are approached, and market objectives remain unmet, alternatives become a necessity. Thus, advanced materials are made using novel structures, quantum dots for example, and different material selections. One of the largest obstructions to this category tends to be environmental factors. Be it rarity or toxicity, either can drive up production costs and interrupt the concept of earth conscientious manufacturing. Navigating a solution to these two problems while finding a compound that still functions as an efficient and viable solar cell absorber is one main direction for current research.

On that note, hybrid solar cells are recently showing some very promising results. Perovskite solar cells can be seen in Figure 1.1 as having exceeded 20% efficiency in the laboratory. As a type of cell that uses organic and inorganic materials for the absorber, spectrum selection for absorption is highly tunable. Still, the presence of Lead gives rise to toxicity concerns, and as with organic solar cells, stability is still an issue.

1.2.2 Economic Outlook

So, with many obstacles and even more options on how to succeed in solving the problem, research pushes forward with goals to one day make solar power have a competitive foothold in the energy supply market.Mertens [13] writes a nice economic outlook expressed as a comparison to other energy forms. A similar but shorter discussion is held in Section 2.2.

1.3 Absorber Synthesis

My focus, in the following presented experimental work, is material synthesis and implementation of synthesized materials into solar cells. Previously, in Section 1.2.1, various architectures were referenced based on the technology used for the absorber layers in the solar cells. Developing a method for determining good absorber layers is important in that the chosen material determines the cell performance possibilities. What methods we use for producing various absorber layers determines how close we can come to reaching the best possible cell for a given material. Using a mechanochemically synthesized nanoparticle layer falls into the emerging technologies category. Later, it should be easier to understand the benefits of choosing such methods, if the means themselves are first understood.

1.3.1 Mechanochemical Synthesis

As might be inferred from the name, a mechanochemical reaction describes a chemical change as a result of mechanical interactions. For example, a flint striker: by applying a suitable amount of mechanical energy to break off small enough pieces of a material such as iron, the small pyrophoric bits ignite in air. This is true of many metals, that an unoxidized small enough particle can ignite due to oxygen exposure. Such is one path available in ball milling. Self-sustaining reactions can take off once appropriate conditions for ignition are met. Slow steady-state reactions [14] and other paths are also available in mechanochemical synthesis. Many of these occur at lower temperatures than bulk solid-state reactions due to various properties of the reactants and conditions in the mill.

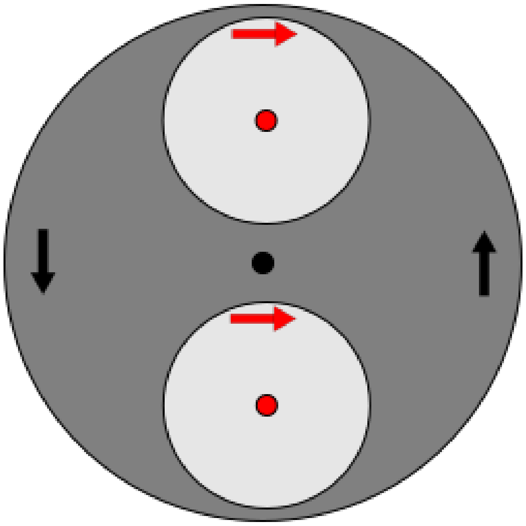

Figure 1.2: Planetary mill rotations in the directions of the color coordinated arrows and axes of rotations.

Ball Milling Parameters

Excluding the chemical reaction, the simple mechanical actions occurring within a planetary ball mill are quite abundant, and these actions vary based on the conditions of a given mill. Forces from pressure, impact, and friction/shearing are some of the main mechanical interactions occurring inside a ball mill. These forces lead to changes in the material, such as deformations, breaking, and agglomerating.

A planetary mill works by rotating cylindrical jars counter to the direction of their rotating platform as illustrated in Figure 1.2. As a result of frictional forces and rotation of the jars about their center, a vortex of the materials should whirl about the center of each jar. However, the platform rotates concurrently with the jars. This leads to centripetal acceleration having two centers, the center of each jar and the platform's rotation center. This means each centripetal force pushes the material differently. One would simply keep everything in a vortex should only the jars spin, and the other would keep material on the outside edge farthest

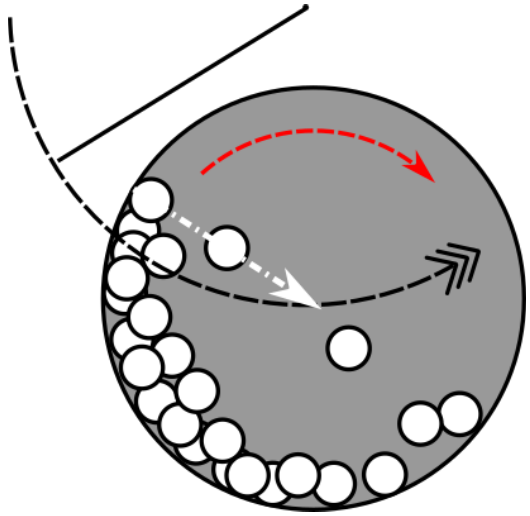

Figure 1.3: Planetary mill mechanics: the black triple arrow path represents the platform rotation, the red arrow path represents the milling jar rotation, and the white arrow path represents the sidewall launch of milling balls and material in the milling jar.

from the platform's rotational center if only the platform rotated. In short, since the acceleration vectors from the two rotations do not always align, the material can fly across the inside of each jar as seen in Figure 1.3. It may be easier to understand these motions in terms of the fictional forces involved. Thus, it may help picture how ball milling works to read on the centrifugal and Coriolis forces, if the motions do not seem intuitive. These fictional forces explain motion observed from a non-inertial frame. These cross collisions are a very important aspect to ball milling, as they are high energy. The frequency and energy of such events can be controlled by various parameters used to control the ball milling outcome.

For the parameters of a milling jar, one can pick various volumes and materials. Though the main reason to used a larger volume jar is to process more material at a time, there could be another reason. The volume ratio of the jar, milling balls, and material changes the frequency and energy of cross jar collisions as shown in Figure 1.3. With a jar more full, energy of collisions decreases due to a shorter mean free path and more matter to absorb the impact. Jar material and milling ball materials can also vary to change impact energy and chemical compatibility. Various available materials have different densities, hardnesses, and elasticities, which effects the energy of collisions. Finally, the milling balls come in various sizes. The smaller ball sizes can reduce final material fineness size minimums, but comes with a trade off of less energy imparted by an individual impact.

Aside from the variables related to the milling jar and balls, there are a few other setup methods to be mentioned. Though one can change the amount of material to be milled in a given run, there are ways to adjust the outcome base on the material preparation. For example, softer materials can be made more brittle by cooling them. Ensuring dried sample preparation for dry milling can keep the mill cleaner and improve product yield. Wet milling is also an option. By increasing the ball ratio, the frictional forces dominate, and adding fluid helps obtain be the best fineness in this scenario. Analogous to this method, a material can be dispersed in a solid medium which will not chemically react with the sample[14, 15]. This can reduce self-agglomeration and improve final fineness. As the reactants are diluted by this process, it can also be advantageous in slowing down the chemical reaction in order to control final product fineness.

Finally, the milling machine has adjustable parameters. Planetary ball mill machines can have various rotation ratios. The Retsch PM 200, used as described in Section 4.1.2, has a ratio of $1 : -2$. Thus, jars complete two revolutions (red arrows in Figure 1.2) during the same time interval as the platform makes one rotation in the opposite direction (black arrows in Figure 1.2). Higher ratios will increase the frequency of cross jar collisions. With a given machine, the revolutions per minute can be adjusted. Due to a higher centripetal acceleration and thus a larger normal force required from the jar wall, faster rotations will increase the pressure and frictional/shearing forces on a material. Also, higher rotations speeds lead to increased collision speed; therefore, the impact energy will also increase. Simply put, dump more energy into the machine and you get a higher energy milling environment. Other useful functions include reversible rotations, which can be programmed to occur at set intervals. This will cause rotational actions of the material inside a jar to change directions, which can cut back on buildup and improve final fineness. Also, rotations can be paused for set intervals. This allows the system to cool, which can lead to a more energy efficient production in certain circumstances. For example, a given material might break down easier when it is cooler. Cooling of hot materials can lead to fracturing, which can also assist in breaking down materials.

The variety in a selection of controllable variables such as the jar, milling balls, filling parameters, and machine settings allow for multiple applications when using a ball mill. Many of these parameters were varied in search of optimal setting for absorber synthesis.

1.4 Characterization

Once materials have been synthesized, it is often standard procedure to characterize the materials in order to assure one has made the intended product. High energy probing allows for a verification process that is fast and simple. Using Scanning Electron Microscopy (SEM) is a fast way to view the morphology of a given material. As various crystals have different lattice structures, the change in dominate geometries can allow visual verification of a chemical change. As the material in question is on the nanoscale, SEM allows the diffraction limitations imposed by light in the visible spectrum to be surpassed. Using SEM allows for more than size and shape visualization. Some other probing methods into chemical structures are available; however, a more specialized piece of equipment allows for similar identification methods to be used with improved accuracy. Namely, analyzing data from X-Ray Powder Diffraction (XRD) gives insight into chemical composition and crystal phase. With these two methods, synthesized materials were examined. Product morphology and chemical composition, post milling reactions, were verified in this way.

1.4.1 Scanning Electron Microscopy (SEM)

As previously mentioned, optically viewing a specimen will only allow for a certain resolution between two points based on a diffraction limit. Since light has wave properties, passing through slit or aperture, such as our pupils, causes diffraction–a spreading of the light wave. When these waves hit a sensor, retina, in the case of our eyes, the ability to discern or distinguish between them has to do with the amount of overlap in the intensity distributions of the waves. Even with magnification, we eventually hit a limit of approximately 300 nanometers due to the wavelength of visible light. For a deeper understanding and more on these calculations, Egerton [16] presents an easy to follow review in his first chapter ”An Introduction to Microscopy.” Our concern, then, is how to observe particles smaller than this limitation. Also, we would like to see features on these small particles. The solution is quite simple, use any probe with a shorter wavelength than visible light.

Electrons that have been accelerated to high enough speeds fulfill our wavelength requirements, as do ultraviolet rays, X-rays, and gamma rays for example. The wavelength can be calculated from the DeBroglie wavelength relationship, as seen in Equation 1.1. The usual physics symbols have been chosen for wavelength, λ, Planck's constant, h, and momentum, p.

$$\lambda = \frac{h}{p} \tag{1.1}$$

If we use energies typically used for SEM to accelerate electrons, then the wavelength will be on the picometer scale [17]. Not only does this mean an improvement in three orders of magnitude, but one may notice this as subatomic in comparison with Ångström order of magnitude for atomic spacing in crystals. Thus, we no longer need to worry as much about our wavelength in determining our resolution like before. Instead, it becomes a matter of how focused the beam width can be made for the electrons, which is still dependent on the wavelength, as well as how the scanning is performed for the image we raster.

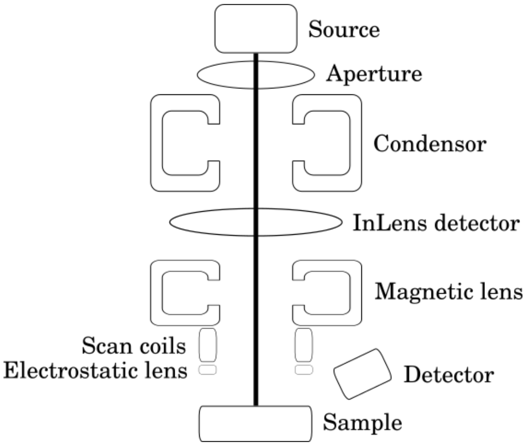

Figure 1.4: An example schematic with components found in a Zeiss Sigma field emission scanning electron microscope as used in this research.

The equipment for SEM has an electron source that supplies the probe beam which is controlled by electrostatic and magnetic fields. For the SEM completed in this research, a field-emission cathode in an electron gun supplies the beam labeled as the “Source” in Figure 1.4. The aperture then clips the beam to the desired width, 30 microns for example. Much like aperture selection in visible light optics for cameras, changing this will change the focusing depth of field for an image as well as the amount of energy going to the sample. Next, the beam is focused onto the sample using magnetic and electrostatic lenses. The scan coils move the beam across an area of the sample in order to raster an image. The image is picked up by a detector of the user’s choice. Electrons scattered from the sample for generating an image are also accompanied by secondary electrons ejected from the sample material, due to the high energy of the incoming beam. These secondary electrons can be used to examine the chemical nature of the sample. Using an Energy-dispersive X-ray (EDX) detector, one can examine the composition and phase of the sample. This is very similar to XRD. Thus, XRD data analysis was the preferred chemical characterization method chosen over EDX spectroscopy in this research.

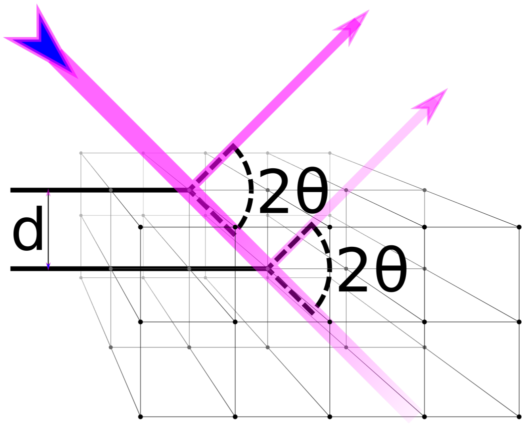

Figure 1.5: Incident rays from the source (blue arrow) scatter from the crystal and head off toward the detector(violet arrows).

1.4.2 X-Ray Powder Diffraction (XRD)

The use of XRD for material characterization includes phase identification along with crystallinity. Quick comparisons to large databases of standard reference patterns allow for identification of samples. This is handled conveniently with visual matching assisted with software recognition and screening. Exploitation of the periodic structures in crystals, the wavelength of X-rays, and Bragg's Law allows for such means to characterization.

In 1912, the three-dimensional diffraction grating properties of a crystalline material were discovered to act on X-rays [18]. This has to do with the periodic structures in crystal lattice spacing and the wavelength of X-rays. As seen in Figure 1.5, scattered light from multiple points in a lattice can move in the same direction to be picked up by a detector. One can visualize each plane as a horizontal array. This diffraction grating like structure will split electromagnetic waves such that various frequencies will scatter at different angles from the surface. Thus, monochromatic X-rays will only scatter at certain angles. The zero order mode (the first observed angle away from the path normal to the plane) will act the same as a reflection. That is to say, the scattered light follows a path away from the

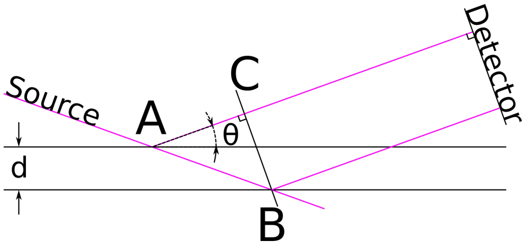

Figure 1.6: Bragg's Law states the condition ($2d\sin\theta = n\lambda$) for which the detector will receive the strongest signal from the scattered rays

plane at an angle equal to incoming light. Usually, the angle used for reflections is the angle of incidence, which is measured normal from the plane; however, in the case of Bragg's Law, the angles are with respect to the planes which contains the scattering points and the respective observational points. So, $\theta = 90^\circ - \theta_{inc}$, where θ is the angle used in Bragg's Law, and θ_{inc} is the angle of incidence used in the law of reflection. This angle is convenient to measure, as the angle between light from the source and light headed to the detector, is 2θ, as seen in Figure 1.5. To put this setup to use, a relation for when the detector will pick up strong signals is necessary. When does the light from two sources constructively add?

For the light coming from two points to add constructively, they must be in phase. Bragg's Law defines the relationship for constructive interference using the distance between planes containing scattering points (d), the angle of light from each plane (θ), and wavelength of the light source (λ) as seen in Figure 1.6. As long as the source is considered to be in phase, then the two paths must differ by an integer multiple of the source wavelength ($n\lambda$) in order to add constructively. Since the paths are parallel from points C and D to the detector, and they both come from the same source, the path difference is the distance $|\vec{AB}| - |\vec{AC}|$.

$$|\vec{AB}| = \frac{d}{\sin(\theta)} \tag{1.2}$$

$$|\vec{AC}| = |\vec{AB}|\cos(2\theta) = \frac{d}{\sin(\theta)}\left(1-2\sin^2(\theta)\right) \tag{1.3}$$

Some simple trigonometry gives the magnitude of each distance in terms of the desired variables. Equation 1.2 uses the definition of the sine function and the right triangle formed with $\vec{AB}$ as the hypotenuse, a vertical side under point A, and base along the bottom plane containing point B in Figure 1.6.Equation 1.3 uses the definition of the cosine function and the right triangle formed with $\vec{AB}$ as the hypotenuse, $\vec{CB}$ as a vertical side, and $\vec{CA}$ as a base, also visible in Figure 1.6. Using the double angle identity $\cos(2\theta) = \left(1-2\sin^2(\theta)\right)$ makes for simple subtraction of $|\vec{AB}| - |\vec{AC}|$. Thus, the path difference set as an integer multiple of the source wavelength gives Bragg's Law, Equation 1.4.

$$\begin{aligned} |\vec{AB}| - |\vec{AC}| &= \frac{d}{\sin(\theta)} - \frac{d}{\sin(\theta)}\left(1-2\sin^2(\theta)\right) = 2d\sin(\theta) \\ \therefore & \\ n\lambda &= 2d\sin(\theta) \qquad (1.4) \end{aligned}$$

Concerns might arise from the two-dimensional derivation of Bragg's Law. However, one can always reduce two vectors in three-dimensional space to two dimensions by moving to the reference plane which both vectors share. If the three-dimensional picture that follows from such transformations becomes unclear, further reading might be useful. Jenkins and Snyder [18] present much of the necessary information in *Introduction to X-ray Powder Diffractometry*. A geometrical approach can be used looking at latices in reciprocal space and seeing the points lying on an Ewald Sphere. Though such depth of knowledge is useful, it is also unnecessary for understanding how X-ray powder diffraction analysis works. All one really needs to understand is that various periodic symmetries exist in a crystal lattice and that these will lead to increased signal intensities at given angles. By mapping the intensity (counts is the common measure) against the angle, while taking measurements through a range of angles, the recorded profile can be distinctly linked to the crystal under observation. Thus, comparisons using large databases full of reference patterns allows for fast, simple phase matching characterization.

1.5 Thin Films

Once material characterization confirmed desired compound synthesis was successful, films which could be used in solar cell prototypes needed to be made. Though solid crystal growth is possible, and some of the leading industry technologies still use these methods, thin film technology allows for less waste. Also, creating a device that is no thicker than necessary allows for a shorter transport distance of the photon generated carriers to their respective electrodes. Ultimately, this leads to getting the best possible device. Therefore, thin film technology will be employed in this research.

Different methods can produce various thin films. One large difference appears when choosing between growing a film onto a substrate versus depositing material onto a substrate. The first option allows for crystalline films, whereas the second choice will inherently suffer from grain boundaries after deposition. However, such methods can have advantages, which were a major factor in deciding to deposit films in this research. It may be easier to discuss such factors following a short background for each method.

1.5.1 Thin Film Growth

When growing thin films, the method builds a film from atoms. Molecular beam epitaxy, vapor deposition, and sputtering are some examples of such methods. Though these methods can be used for physical deposition and need not be chemical, in this section the focus is film growth. Films can also be grown from solutions; however, such methods do not tend to lead to crystalline films, the main benefit in film growth.

Molecular beam epitaxy essentially allows atomic level control of crystal growth from vapor phase reactants. The controlled environment leads to some of the most crystalline samples available for artificial crystal growth. The largest downside comes from the amount of time needed to grow material and the cost. The expense in this choice comes from the ultrahigh vacuum environment and the difficulty in using the equipment.

Chemical vapor deposition can similarly grow crystals from vapor phase reactants. The chambers can be at atmospheric pressure, low-pressure, or ultrahigh vacuum environments. Depending on the requirements, this can save on cost. However, the purity of grown films can suffer. The gas flow in the chamber allows for reactants to drift and deposit onto a substrate, as opposed to the gas beam of reactants being directed at the substrate as done in molecular beam epitaxy.

Sputtering hits a target, which then ejects some material toward the substrate for deposition. What is used to hit the target will change how the deposition on the substrate happens. A source could be plasma, ions, inert gasses, or reactive gasses for example. This can mean the target can travel to the substrate and hit in a vapor or liquid phase. Also, the reactive gasses allow for reactions to happen before the deposition on the substrate. Thus, epitaxial growth is possible as well as physical deposition. Again, equipment complexity leads to a rise in cost for film growth. Thus, let us look at some top-down approaches to thin films as opposed to the bottom-up growth of films.

1.5.2 Thin Film Deposition

Instead of chemically forming a film, as in epitaxial growth, let us start with a finished product and then find a way to make a film. It has already been mentioned that such depositions are possible with physical vapor deposition, and sputtering; however, let us look instead at some lower temperature options. For example, a suspension or colloid is prepared by using small particles of the desired compound dispersed in a liquid. This colloid is then dispensed on the substrate for the thin film. Some examples include using rollers or doctor blading; as well as spray, dip, and spin coating; and drop casting.

The first two methods simply spread the colloid onto a substrate mechanically. The thickness of applied colloid is thus controlled by the mechanics of the process–be it a blade, roller, or another mechanism which removes excess colloid. With the evaporation of the liquid, a film is left on the substrate.

Spray coating can be done hot, such as spraying solids which have been melted to their liquid phase. However, spray coating done at lower temperatures, such as will be discussed, has mechanisms for film formation which differ slightly. Adhesion of the product in a colloid to the substrate requires a certain impact speed. So, the spraying mist controls the amount of colloid dispensed, but the impact of the spray also plays a role in the final film. Again, evaporation of the liquid leaves behind the desired film.

The remaining methods rely on surface tension to determine the amount of dispensed colloid. In dip coating, adhesion holds the colloid to the substrate as it is removed from its submersion. Then, cohesion pulls more colloid along with the amount stuck to the surface. Thus, there is an upward flow of colloid with the substrate rising and an outward flow where excess fluid is returning. The stagnation point, where the flow is zero, determines the thickness. The balancing of these forces is due to the surface tension. Also, viscosity and density of the colloid play a roll. Since viscosity is a resistance to the flow, it will affect flow of the colloid in all directions. Density will change the forces felt by gravity, which support the flow back into the colloid reservoir.

Spin coating is similar to dip coating, but the lack of enough centripetal force holding the colloid in a lateral direction toward the center of rotation results in the loss of colloid. This is similar to how gravity pulls the colloid off of the substrate in dip coating. However, the acceleration due to spinning can be many times that of gravity, so the colloid will be pressed thinner to the substrate in comparison with dip coating. Also, this pressing action compresses the film. For these two reasons along with speed and simplicity of adjustments, spin coating was one of the methods employed in this research along with drop casting.

Drop casting is similar to spray coating, in that the amount of colloid on the substrate will determine the film thickness. However, this method leaves the least uniform films. An advantage is that drop casting is quick, simple, and can make moderately thick films in a single coat. As empirical methods lead to choosing this method, more will be discussed in Section 5.2.

1.5.3 Film Characterization

As various films were made, it was important to quantify some of the differences. Visual inspection allowed for qualitative and semi-quantitative measures on film uniformity and thickness. As the final objective is a working solar cell prototype, quantitative optical and electrical measurements help in ascertaining the viability of a given film.

Absorption, Transmission, and Reflectance

The idea behind solar cell energy harvesting relies on absorbing photons from the sun and collecting carriers separated by such an absorption. Thus, it is a good idea to check how much light, from the sun, a material is capable of absorbing. This can give the relevant band gap of the material in observation of the absorption onset. It can help in determining a necessary thickness of material in order to mostly absorb the sunlight. When layering materials, it can help with deciding the layer order based off of what light will be transmitted through a given material. In short, absorption, transmission, and reflection data are useful in the architectural design of a solar cell.

When light hits material it can scatter, transmit, or be absorbed. There are pieces of equipment that will measure transmittance, as well as spectral and diffuse reflections. With this, absorption is what is left over. Since reflections are elastic scattering, one can think of a nominal value coming off of with transmission spectrum from 100% and the remainder is absorption. Thus, the characteristic shape will be the same, but the value will differ.

Though keeping the incident angle of zero for transmission measurements ensures such a relation, no such perfect scenarios exist. Thus, using equipment that measures both transmission and scattering is more accurate. This accuracy cost more time and money, and it serves little purpose at prototype development stages. So, characterization of films is carried out only with transmission measurements, as outlined in Section 5.3.

Current Versus Potential

As the ultimate goal of solar energy harvest is power supply from sunlight, it is good to gauge how much power is available from a solar cell. This is done by measuring the current generated at various potentials in the influence of light. Measuring the same output in the dark can lead to useful information about a successful solar cell.

When illuminated, the current measurements taken at various potentials can give all the necessary information for power generation capabilities. Refer to Figure 1.7 for a visual indication of the important parameters to be measured.

The open circuit potential (V_{oc}) is the point where zero current is measured. This means the photopotential is equal and opposite to the applied potential at this point. The current measured when there is no applied potential is the short circuit current (I_{sc}). This is the largest possible current the cell can supply. If there were no resistive losses, the power possible would be the product of the open circuit potential and the short circuit current. By integrating the current with respect to the potential, we can find the largest power value (P_{max}). This is visualized as the largest area box that can be drawn in the current versus potential curve as seen in Figure 1.7. The current (I_{mp}) and the potential (V_{mp}) at the maximum power output are important in how a cell can be implemented when supplying power to devices. Experimental current versus potential measurements are discussed in Section 5.4.

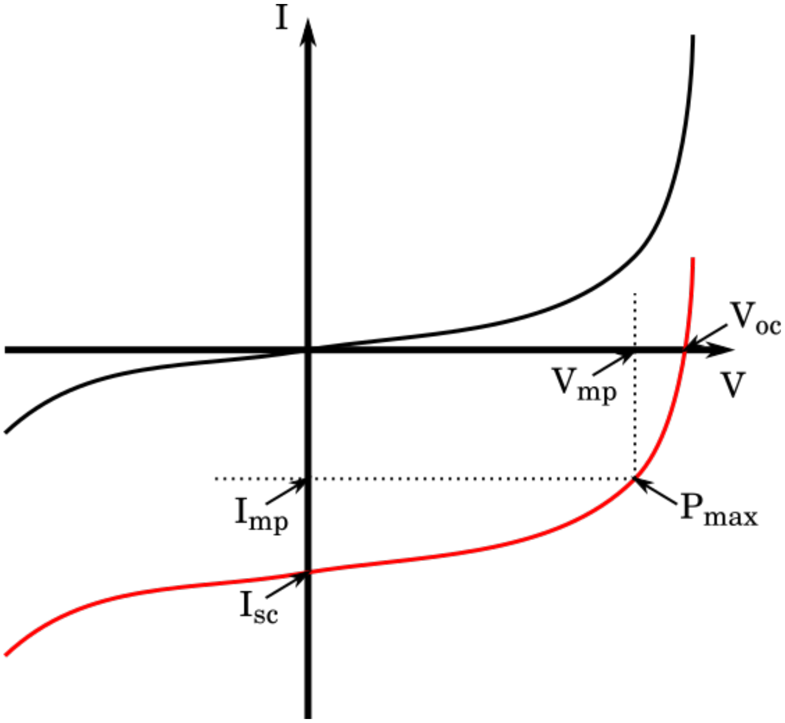

Figure 1.7: Typical current (I) versus potential (V) graph for solar cells. The curve in black represents the dark current measurement and the curve in red is the illuminated measurement.

Chapter 2

Motivation for Solar Cells

Environmental and economic demands are initiating growth in solar cell technology. With growing financial investments, social awareness, research, and various other forms of support much can be realized in solar cell implementation.

Science must answer the call for clean energy. The health of current and future generations relies on the innovation of researchers for providing solutions to current global health concerns. A quick overview regarding some of the largest areas of concern for health can be viewed in Figure 2.1. A very straight forward approach to solving some of these issues is to provide clean energy. Also, a quick glance shows that the developing countries clearly suffer most. Thus, economical solutions stand to make the largest global impact.

2.1 Environmental Solutions

Many issues surrounding the general well-being of those currently living in the world can be addressed with cheap clean energy. According to the World Health Organization [20],

> Air pollution causes 1 in 9 deaths. It is the biggest environmental health crisis we face.

As already mentioned, in reference to *The World Health Report 2002–Reducing*

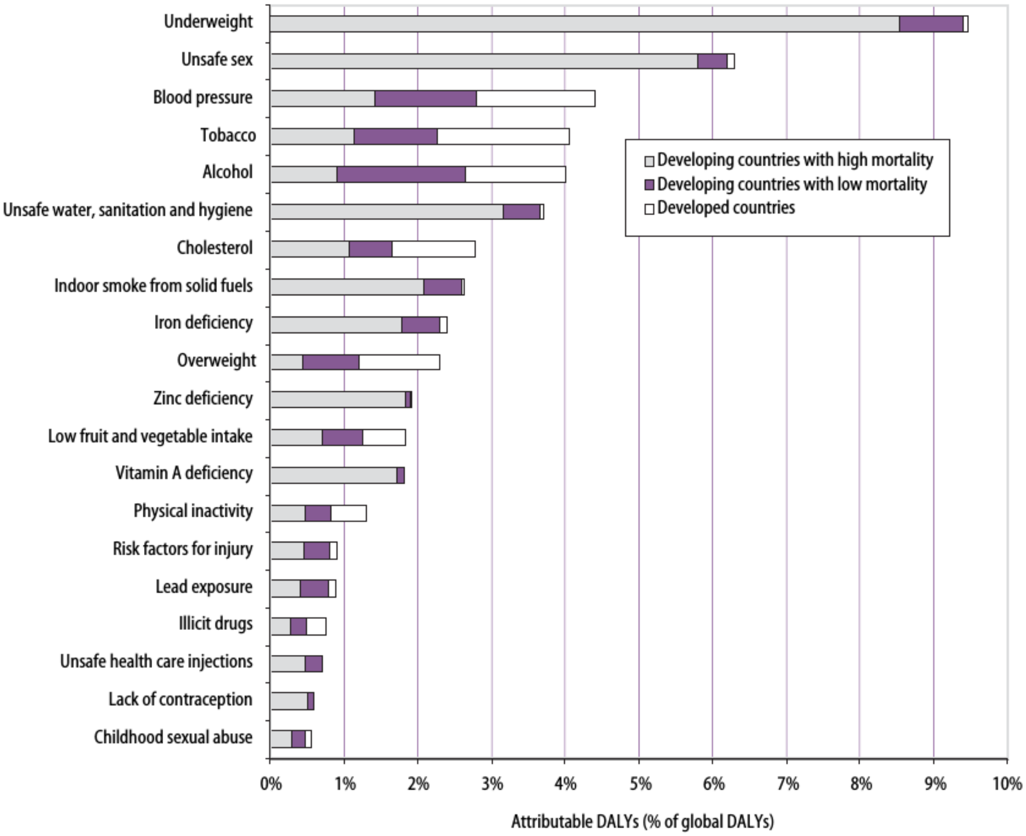

Figure 2.1: A "global distribution of burden of disease attributable to 20 leading selected risk factors" in units of disability-adjusted life years (DALYs) by the World Health Organization [19].

Risks, Promoting Healthy Life, one can view some of the major health concerns in Figure 2.1. Currently, approximately 3 million people die each year from outdoor air pollution and approximately 4.3 million from indoor air pollution [20]. Thus, collectively, outdoor and indoor, air pollution can be viewed as one of the largest burdens on life. A majority of the pollutants come from energy sources, namely fuels, in supporting various daily needs: cooking, heating, transportation, et cetera. Since many of these tasks have electrical alternatives, a solution exists where clean affordable energy supplants the need for other energy sources. This includes a need to replace large power stations which rely on fuels. Opinions eventually become ethics if enough people agree, and the United Nations, comprised of 193 Member States, is pushing for this very change. As of January 1, 2016, *Transforming our world: the 2030 Agenda for Sustainable Development*, a layout of 17 sustainability goals are in effect[21]. Along with the aforementioned health issues, this agenda also addresses environmental concerns for the planet.

The impact left by many of the air pollutants has led to noticeable climate changes. Also, many of the fuel sources are non-renewable. For some renewable resources, deforestation as an example, trees are not being replenished at the rate we are using them. Awareness of the footprint left behind by our current decisions has become a more socially necessary step in all fields; videlicet, research, business, government, and other aspects of life require earth conscientious decisions. As solar energy is diurnally abundant well beyond any foreseeable near future needs, visually apparent in Figure 2.2, the only environmental concerns become the production and implementation of solar cells.

2.2 Economic Opportunity

An environmental push is not all that has motivated growth in solar energy harvesting technologies. Many modern devices requiring electrical power have usage demands. Though battery technologies have made longer use possible while maintaining or decreasing size and weight, other options have helped motivate novel solar cell applications. Combining effects from various factors: government efforts, industrial large-scale installations, wearable device popularity, and other financial endeavors, has lead solar generated power to finally reach competitive sales values with other energy technologies.

Early adoption of solar cells in devices included watches, calculators, and various personal devices. With more modern versions such as Eco-Drive watches, Misfit Wearables, and other such devices, solar power has not left the wearable technology market. Though it lags behind the novelty industry in terms of current financial investment, medical wearable devices are also adding to the demand pool

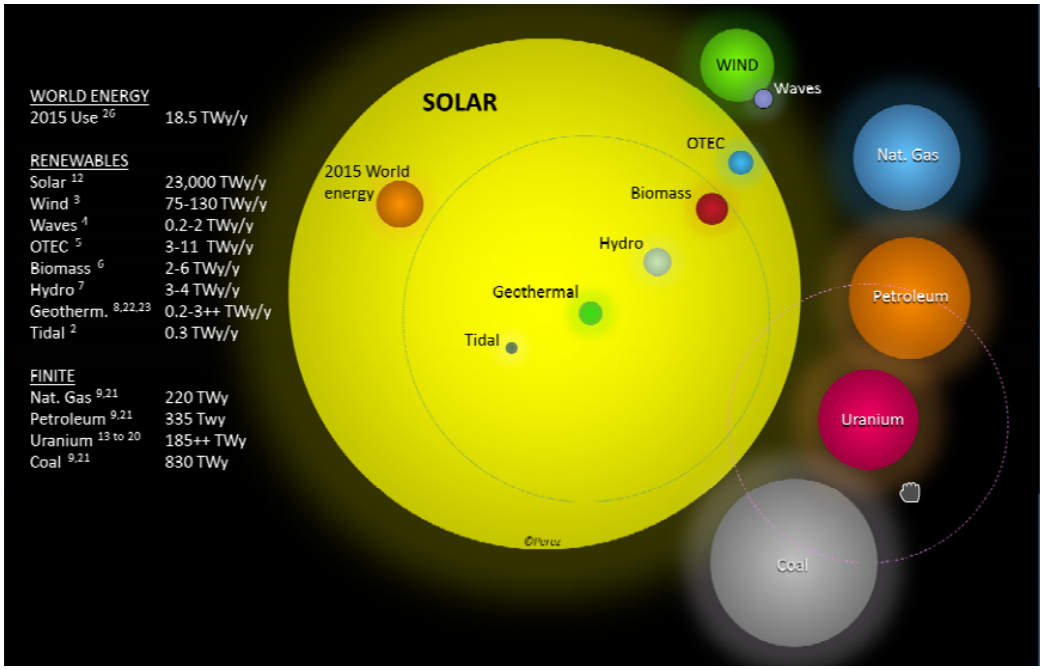

Figure 2.2: "2015 estimated finite and renewable planetary energy reserves (Terawatt-years). Total recoverable reserves are shown for the finite resources. Yearly potential is shown for the renewables." A visual representation by sphere volume size from Perez and Perez [22].

for better technologies. These niche groups are an example of how every little bit helps. Their investments will continue to make an impact on the production costs associated with solar energy harvesting technologies.

On a larger scale, government policies such as various subsidy projects and tax incentives for installations all have made a noticeable pricing impact. Solar power stations are going up around the world and project bidding has continually driven down the price of solar cell modules. The goals laid out in 2011, for the year 2020, by SunShot [23] ($0.09 per kilowatt-hour for residential solar, $0.07 per kilowatt-hour for commercial solar, and $0.06 per kilowatt hour for utility-scale solar localized cost of electricity pricing) have been more than 90% met as of November 2016.

Large corporations pledging 100% renewable energy operations has helped in funding such endeavors. Tesla, Panasonic, and Solar City have come together in making a roof that integrates solar cells. The roofs for 2017 are supposedly going to be cheaper to install than a standard new roof. Competitive entrepreneurial moves such as this will also continue to drive down the cost of solar energy harvesting.

2.3 Nanotechnology Benefits

With so many environmental and economic incentives, emerging technologies are everywhere in solar cell related research. In order to compete with current solar cell technologies, new designs must have the means to supersede existing devices. This means passing current price per performance measures or having the possibility to do so.

Nanotechnologies are a gateway to new solar cell performance properties. For example, colloidal solutions which employ nanocrystals allow for cheap deposition methods on a large scale, such as roll-to-roll coatings. Nanocrystals can be band gap tuned based on their size. Also, using thin cell layers has possibilities in cost savings and performance enhancement for a solar cell. That is to say, less material used can mean lower costs and an appropriate layer thickness can be optimized for a given cell structure's architecture, which in turn improves the overall solar cell performance.

Also, nanotechnologies open possibilities in the realm of small device applications. As the overall structure becomes thin enough, flexible electronic applications become realizable. Likewise, the inherent nature of having nanoscale components is a viable microscopic device opportunity. Thus, the mere size of nanotechnological devices creates an avenue for implementation into novel products.

Many mechanical, electrical, and optical characteristics can benefit from nanotechnological properties of materials. Smaller components are more thermodynamically favorable. That is due to their surface area to volume ratio increasing with decreasing size. For this same reason, access to photogenerated carriers can improve, which can lead to enhanced solar cell performance. Also, at small enough sizes, quantum mechanical properties become apparent in materials. One benefit of this is that it tends to improve the optical absorption characteristics of the material.

2.4 Previous Works

With all the opportunities and reasons for solar cell research, there is usually nothing more than a small change from previous works in order to try and improve the current status of a given research project. After sorting through many designs in emerging technologies, I set some research boundaries. Prototype designs should maintain an earth conscientious design while producing a near future possibility of implementation. This means to me that the technology implored should be easily scalable and cost effective. The raw resources used should be abundant and safe. For these reasons and those given in some of the following literature, Fe_2GeS_4 was chosen as an absorber compound.

This compound received attention as early as 1976 with a paper on the crystal structure by Vincent et al. [24], and later gained some more interest in other papers [25, 26]. However, Oregon State University seems to be the first to recognize the potential of Fe_2GeS_4 as a solar cell absorber material.

Spies [27] recognized the potential of the material, measuring favorable values for the band gap, conductivity, and Seebeck coefficient; however, sputtering a film was not successful. Platt [28], who Spies [27] thanks in his thesis, added to the previously mentioned data with a transmission spectrum from a single crystal, electron microprobe analysis of pellets, and theory calculations of band structures and the absorption coefficient using Wien2K. Then, in 2011, Yu et al. [29] write a summary of the current findings supporting the use of Fe_2GeS_4 as a solar cell absorber material. Pelatt [30] mentions the United States National Renewable Energy Laboratory's calculation of a 21% efficiency possibility for Fe_2GeS_4 using the spectroscopic limited maximum efficiency metric. The films he sputtered suffered from oxygen contamination and extension of previous film characterization included absorption and hall measurements. Finally, Ravichandran [31] wraps up the currently available work done at Oregon State University. His theory work was mentioned by Pelatt [30], and it supports a drift based design using Fe_2GeS_4 as an absorber. Using sputtered films, which again suffered from oxygen contamination, photoelectrochemical cell measurements showed a photocurrent, but no photopotential. A possible photopotential was extrapolated using photoluminescence data. With these new measurements and preexisting measurements, various device simulations were conducted. Other work, done under the United States Department of Energy, includes work done at Colorado State University. Fredrick and Prieto [32] report a solution synthesis preparation for a doctor bladed film. To date, the best cell performance had a 6 mV open circuit potential and $0.3\ \mathrm{mA \cdot cm^{-2}}$ current density.

Outside of the United States, this compound has also seen attention in Korea. Park et al. [33] have done a mechanochemical synthesis of Fe_2GeS_4, leaving options open for possibly easy implementation of nanoparticles into a thin solar cell. There has also been a one-pot production method used to produce nanosheets [34].

With the influence of these works, it seemed probable that a mechanochemical synthesis could alleviate delamination and stoichiometry problems arising during sputtering. That is to say, germanium likes to alloy with many materials. Thus, high heat deposition onto metal substrates leads to delamination and the compound does not stick to the substrate. Also, the sputtering tended to require post treatment to fix stoichiometry problems with the deposition. Since the stoichiometry is easy to control with mechanochemical synthesis and the low-temperature deposition of nanoparticles does not change this stoichiometry. Both problems would appear to have a solution, which will be investigated by this research. Also, one might avoid organic compound contamination from solution synthesis. As no current theory seems to model mechanochemical reactions in an experimentally useful way, a new model was developed in Chapter 3 with hopes to one day be able to optimize mechanochemical processes with theoretical assistance. Experimental works are presented in Chapters 4 and 5.

Chapter 3

Modelling

An adaptable model focused on generality will be presented to address the current lack of well-defined parameters in solid state chemistry. A few sample curves roughly matched to temporal experimental data demonstrates the feasibility of the model. The data necessary for completely modeling the synthesis of Fe_2GeS_4 is in excess of the current goal. One example of a future use for such a model would be optimizing the material synthesis processes through adjusting milling parameters to correspond with the optimal points seen in the model. Here an explanation on appropriately adjusting parameters to fit data with the real world parameters should allow others to understand the model and implement it as best fits their needs. In short, the logic for why a model was written: eventual optimization possibilities for minimizing manufacturing costs, as well as enhancement of general scientific understanding for a relatively archaic system, and separation of physically measurable parameters for that system.

3.1 Application of the Model

A logical combination of various parameters is achieved via sigmoid function coefficients for terms within the system. The ternary, Fe_2GeS_4, to be used as an absorber in a solar cell, has been used as an example for an application of the model.

Currently, there exist models based on mechanochemical processes from the viewpoint of thermodynamics [35], and other chemical analysis means. As well, physical models, which track the mechanics of the process [36] are plentiful; however, the two ideas integrated in a meaningful and useful way still needs to emerge. This area of solid state chemical kinetics is heavily under-represented because the problem contains so many dynamic parameters.

For example, some chemical kinetics models use a mass fraction function in a differential reaction model [37–39]. The mass fraction models are selected to fit the reaction profile; however, this leaves many shortcomings in understanding the reaction. The many variables in an experiment (i.e. temperature, concentrations, particle sizes, and morphology) all change the same parameters for the reaction (order, rate, and induction time) [40].

The goal here is to develop a model which incorporates the synthesis chemistry, physical parameters, and the energy input for the synthesis all in one model. Individually, these can become large-scale arcane models. Unless written as a whole software program, to implement the models with a nice simple graphical user interface, such an approach serves little purpose for industry or experimentalists. Thus, this goal must also maintain reasonable simplicity in the development of a usable model, which can allow for expansion as necessary. Such a model is developed in Section 3.2, presented step by step as a demonstration in Section 3.3, applied to a proof of principle in Section 3.4. Extended application ideas for the model are discussed in Chapter 6.

3.2 Modelling the Chemistry of Ball Milling

Many techniques can be utilized in modeling ball milling synthesis and have names; videlicet, thermodynamics, fluid mechanics, classical mechanics, solid state physics, statistical mechanics, and many other fields provide useful tools. With mathematical overlap in these fields, much can be realized through starting with an overly simplified model. Then, additions can be made to the model as necessary to form a usable and versatile model.

For a starting point, the chemical reactions will be modeled as done in chemical dynamics, where the rate of reaction is related to the product of the reactants. That is to say, the rate of change for a compound within a system is proportional to the statistical interactions of the elements in the system which form the compound. Though this has past been considered irrelevant, as typically solid state reactions are governed more by the available interaction surface. Thus, diffusion is often the main rate-limiting step; however, merit can still come from this decision. After all, the goal includes a generalized model, which does not only work for solids. Also, powders can be modeled as fluids under certain circumstances, as done by Hao [41]. In milling, as nanoparticles approach molecular sizes and local temperatures lead to sublimation of solids, gas related chemical dynamics cannot be ignored. So, some logic to decide how close the reaction lies to either end of the spectrum (solids versus fluids) becomes useful.

One parameter to control the statistical outcome of interactions in such a system is the coefficients used for the interactions. Sigmoid functions can work in this way, allowing a probabilistic or fuzzy, logic approach for choosing which end of a continual logic distribution the reaction will proceed. These coefficients are integrals of pulse functions (i.e. arctangent). Said another way, the derivative of the coefficient should be a pulse function. This allows a cap, such as a maximum reaction rate. For this model, this is the chemical reaction rate as a gas. Thus, the maximum rate would be the expected chemical reaction rate achieved if the appropriate reactants collide with the correct energy. This is chemical kinetics without consideration for solid properties. Then this rate will diminish as the surface area to volume ratio of a solid particle decreases. The model will be built up in this fashion, starting from a basic interaction model.

3.2.1 Interaction Model

Before diving directly into writing differential equations for the elements within the system, it would be useful to address which chemical reactions will be considered in the example. According to Yu et al. [29], the enthalpy of Fe_2GeS_4 formation from the binaries, as seen in Equation (3.3), is positive. Therefore, the ternary is more stable than the binaries. In the spirit of this statement, a two stage reaction from the base elements to these binaries (Equations (3.1) and (3.2)) followed by the aforementioned reaction will be used.

Chemical Reaction Formulas

$$Fe^{2+} + S^{2-} \leftrightharpoons FeS \tag{3.1}$$

$$Ge^{4+} + 2S^{2-} \leftrightharpoons GeS_2 \tag{3.2}$$

$$2FeS + GeS_2 \leftrightharpoons Fe_2GeS_4 \tag{3.3}$$

Instead of starting with chemical kinetics, first look at the continuous model in a discretized manner in order to understand the stoichiometric balancing. A brief inspection of the reactants in Equations (3.1) to (3.3) will lead to Equations (3.4) to (3.9). In detail: the forward reaction in Equation (3.1) can be thought of as one of each reactant is lost to form one product. So, by bringing the two reactants together, one of each is lost and the product is formed. These interaction terms (the product of two elements of the system) are seen as the negative terms (-[Fe][S]) in the rates given in Equations (3.4) and (3.6). Next, in Equation (3.2), one Germanium ion and two Sulfur ions are lost to form one product. These product terms are unlike the previous ones in that Sulfur loses two ions. Thus, the interaction term (-[Ge][S]) has a coefficient of one for Germanium Equation (3.5)), and receives a coefficient of two for Sulfur (Equation (3.6)). Using this logic, it becomes apparent how to build an interaction model (Equations (3.4) to (3.9)) from the chemical reaction formulas (Equations (3.1) to (3.3)).

Interaction Model Equations

$$\frac{\partial Fe}{\partial t} = -[Fe][S] \tag{3.4}$$

$$\frac{\partial Ge}{\partial t} = -[Ge][S] \tag{3.5}$$

$$\frac{\partial S}{\partial t} = -[Fe][S] - 2[Ge][S] \tag{3.6}$$

$$\frac{\partial FeS}{\partial t} = [Fe][S] - 2[FeS][GeS_2] \tag{3.7}$$

$$\frac{\partial GeS_2}{\partial t} = [Ge][S] - [FeS][GeS_2] \tag{3.8}$$

$$\frac{\partial Fe_2GeS_4}{\partial t} = [FeS][GeS_2] \tag{3.9}$$

3.2.2 Chemical Kinetics Model

The equations of the interaction model need some extra input for chemical kinetics. This information comes from the field of chemical dynamics. Chemical dynamics studies the mechanisms behind reaction rates. The approach is to use concentrations. This is typically applied to fluids (gasses and liquids); however, as previously mentioned, powders can be viewed as a fluid for some applications.

One of the standard views is to think of an ideal gas reaction based on collision probabilities. If a molecule exists in a given volume, the odds of finding it in the given space is the quotient of the molecule volume over the entire space volume. This is essentially concentration if the units used to represent the molecule and space are chosen properly and the volume of an individual molecule is small in comparison to that space. Combine this with basic statistics for a coincident event of two probabilistic events (i.e. finding molecule A in space C out of volume D at the same time as finding molecule B in space C out of volume D) and one realizes the event occurs with the product of the concentrations ($\frac{AC}{D} \times \frac{BC}{D}$). In order to properly treat such cases, this becomes a statistical mechanics problem where the electrons in the bonds become the focus. This is one reason, only the simplest reactions can be modeled computationally for reaction rates.

> “One of the observations regarding the study of reaction rates is that a rate cannot be calculated from first principles. Theory is not developed to the point where it is possible to calculate how fast most reactions will take place. For some very simple gas phase reactions, it is possible to calculate approximately how fast the reaction should take place, but details of the process must usually be determined experimentally. Chemical kinetics is largely an experimental science [42].”

With this in mind, though the equations remain empirical, efforts are made to organize coefficients in a fashion to allow for ease of use and understanding when matching the parameters with experimental measurements. As well as in the previous model, chemical kinetics relates the rate of a chemical reaction to the rates of all the reactants by the negative inverse of their chemical reaction formula coefficient and the positive inverse for the products. Though this is done as shown in Equations (3.10) to (3.12), the reason to start with an interaction model is hopefully apparent. Correctly using these three reactions which all have coupled rates can become an accidental mess pretty quick.

$$\text{Chemical Reaction Equation (3.1) Rate} = -\frac{\partial Fe}{\partial t} = -\frac{\partial S}{\partial t} = \frac{\partial FeS}{\partial t} \tag{3.10}$$

$$\text{Chemical Reaction Equation (3.2) Rate} = -\frac{\partial Ge}{\partial t} = -\frac{1}{2}\frac{\partial S}{\partial t} = \frac{\partial GeS_2}{\partial t} \tag{3.11}$$

Chemical Reaction Equation (3.3) Rate = (3.12)

$$-\frac{1}{2}\frac{\partial FeS}{\partial t} = -\frac{\partial GeS_2}{\partial t} = \frac{\partial Fe_2GeS_4}{\partial t}$$

Another variation from the interaction model was the change in the orders of the reactions and the addition of rate coefficients. The reaction orders come directly from the probability view mentioned previously. This is not the case for all reactions, but for many elementary reactions with no intermediary steps, this is a good starting guess. This is the reason for modeling the example reaction as multiple elementary reactions. If modeled as a reaction from the starting elements to the final product, then an intermediary step could contain unknown information, but this could not be gained by skipping these steps. This is less of a concern when listing all the steps as elementary reactions.

The other concern to be addressed before moving on is the reason for using the three reactions chosen. For justification of this decision: the previously mentioned reference by Yu et al. [29]; along with experimental observations where FeS is found in the incomplete reactions of the product; and similar findings by Park et al. [33] who previously synthesized the compound via ball milling, all support such a model. There are other possible paths, but upon further investigation, they contained less stable derivatives compared to the ones used in these steps.

As a final note, coefficients for the reaction rates function as a fitting parameter in Equations (3.13) to (3.18). These are three separate coefficients as we have three reaction rates (Equations (3.10) to (3.12)), and they may or may not happen at the same speed. As stated, these formulas get used empirically in the long run, which includes needing to know how fast a reaction occurs while limiting the variable parameters involved in the reaction. Though these coefficients have some pre-existing empirical relations that can be correlated to physical parameters, development of this model is independent of such approaches. The reason being that the current models simply relate each coefficient to an exponential or product of exponential functions, as that is the form of the solution to the first order reaction. Then, they leave the coefficient in front as a dynamic fitting parameter. Again, that really only holds significant meaning for certain first order reactions.

> “As we consider a few types of solid state reactions, we will see that there is no simple interpretation of k possible in some instances [42].”

Chemical Kinetics Model Equations

$$\frac{\partial Fe}{\partial t} = -k_{FeS}[Fe][S] \tag{3.13}$$

$$\frac{\partial Ge}{\partial t} = -k_{GeS_2}[Ge][S]^2 \tag{3.14}$$

$$\frac{\partial S}{\partial t} = -k_{FeS}[Fe][S] - 2k_{GeS_2}[Ge][S]^2 \tag{3.15}$$

$$\frac{\partial FeS}{\partial t} = k_{FeS}[Fe][S] - 2k_{Fe_2GeS_4}[FeS]^2[GeS_2] \tag{3.16}$$

$$\frac{\partial GeS_2}{\partial t} = k_{GeS_2}[Ge][S] - k_{Fe_2GeS_4}[FeS]^2[GeS_2] \tag{3.17}$$

$$\frac{\partial Fe_2GeS_4}{\partial t} = k_{Fe_2GeS_4}[FeS]^2[GeS_2] \tag{3.18}$$

As an alternative to trying to make this type of form which comes from the solutions, where the meaning behind the model quickly gets lost in the mathematics for most people, instead break up the coefficients in a more direct way. For those comfortable with differential equations, this will remain as clear as the interaction model. Another reason is to be more explicit in the dependencies in a way that fits well to the experimental data.

For the typical approach to the problem, one notes the steady state solution–the ratios of the product over the reactants is constant at thermodynamic equilibrium.

This is the thermodynamic approach, to which one can relate this to Gibbs free energy. Assume a Boltzmann distribution of your molecules to correlate with the speed of the molecules. Then, you get the typical Gibbs energy solution, which then takes the form of the Arrhenius equation if you relate the change in Gibbs free energy to the change in enthalpy.

To this end, energy dependence is one major parameter. In favor of not stating energy as a proportionality by using a dynamic coefficient and a Boltzmann energy distribution, stick with a probability approach. This will still take on the form of multiplying the coefficients where large scale problem is described by various coefficients, but in a normalized (in the range of 0-100%) manner.

3.2.3 Effective Reaction Area Terms in the Chemical Kinetics Model

In mechanochemical processes, such as ball milling, materials are made to react through an application of mechanical force. The molecules collide and a chemical change occurs on the outer surface of the particles or at dislocations. Even in the event of a self-sustained thermally driven process, it happens in a way that the reaction locations can be considered to occur over some functional area. The example case, as an exothermic reaction releasing energy during the formation of Fe_2GeS_4, seen in Equation (3.3), proceeds in such a way. Since the chemical reaction speed maximum is already implemented through other coefficients, the next focus on size dependence is a concept of effective area dependence.

To this end, a coefficient that increases as more available molecules in the particle can react will be an effective reaction area related term. The range of arctangent is from $-\frac{\pi}{2}$ to $\frac{\pi}{2}$. So, the sigmoid normalized coefficient, as shown in Equation (3.19), will be arctangent. Other sigmoid options are viable, this is one example. By dividing the arctangent function by π and adding one-half, the range of goes from zero to one, just as desired. For simplicity of the example, imagine a particle as a sphere. Thus, the surface area is proportional to the particle radius (R_i), which decreases at some rate (k_{i_R}) as milling proceeds (Equation (3.20)).

At some critical effective reaction area ($R_{i_{crit}}$), the induction period begins, the coefficient as a function of the particle radius, reaches an inflection (the slope goes from positive increasing to positive decreasing) and a value of one-half. How quickly the value changes from near zero to near one depends on the set width (W_i). In the limit of $W_i \to \infty$ this becomes instantaneous (the Heaviside function). This allows insight to size dependence of the reaction. If the reaction is heavily dependent on some critical particle size, the value becomes immense. However, if the reaction is continually taking place, but simply occurs more efficiently at some critical size, the value will be lower. This allows us to easily fit the model to empirical data from particle size and to understand the dependence.

$$R_{i_{dep}} = \frac{1}{2} + \frac{\arctan(W_i(R_{i_{crit}} - R_i))}{\pi} \tag{3.19}$$

$$\frac{dR_i}{dt} = k_{i_R} \tag{3.20}$$

As a side note, R_i need not be a radius, it was merely convenient notation. All that really matters is picking some variable which can easily be correlated to particle size and effective reaction area–so as to readily understand the size dependence of the reaction. Another notation convenience was keeping all the same k_i reaction coefficients in Equations (3.21) to (3.26) as listed in Equations (3.13) to (3.18). This can be taken a few ways. Preferably, interpret the dependencies coming out of the coefficient. In other words, the k_i reaction coefficients in Equations (3.13) to (3.18) contain the information of the k_i (which should be k_i') reaction coefficients in Equations (3.21) to (3.26) such that $k_i = R_{i_{dep}} k_i'$. In this fashion, one can continue understanding more about individual dependencies for a reaction, instead of all dependencies lumping into one dynamic coefficient. The final goal, if achievable, is an expression where all dependencies are listed. Then, a fitting parameter (k_i) becomes nothing more than a normalizing constant, unvarying with any reaction parameters, because all dynamic dependencies are clearly listed in other terms.

Effective Reaction Area Terms in the Chemical Kinetics Model Equations

$$\frac{\partial Fe}{\partial t} = -R_{Fe_{dep}} R_{S_{dep}} k_{FeS} [Fe][S] \tag{3.21}$$

$$\frac{\partial Ge}{\partial t} = -R_{Ge_{dep}} R_{S_{dep}} k_{GeS_2} [Ge][S]^2 \tag{3.22}$$

$$\begin{aligned} \frac{\partial S}{\partial t} = &-R_{Fe_{dep}} R_{S_{dep}} k_{FeS} [Fe][S] \\ &-2R_{Ge_{dep}} R_{S_{dep}} k_{GeS_2} [Ge][S]^2 \end{aligned} \tag{3.23}$$

$$\begin{aligned} \frac{\partial FeS}{\partial t} = &R_{Fe_{dep}} R_{S_{dep}} k_{FeS} [Fe][S] \\ &-2R_{FeS_{dep}} R_{GeS_{2dep}} k_{Fe_2GeS_4} [FeS]^2 [GeS_2] \end{aligned} \tag{3.24}$$

$$\begin{aligned} \frac{\partial GeS_2}{\partial t} = &R_{Ge_{dep}} R_{S_{dep}} k_{GeS_2} [Ge][S] \\ &-R_{FeS_{dep}} R_{GeS_{2dep}} k_{Fe_2GeS_4} [FeS]^2 [GeS_2] \end{aligned} \tag{3.25}$$

$$\frac{\partial Fe_2GeS_4}{\partial t} = R_{FeS_{dep}} R_{GeS_{2dep}} k_{Fe_2GeS_4} [FeS]^2 [GeS_2] \tag{3.26}$$

3.2.4 Energy Dependent Terms in the Chemical Kinetics Model

The final step, of this model, is to add in energy dependence. So far, reaction probability based on collisions, and availability of those reactions based on an effective reaction area are included. What of energy? Temperature, mechanical input, and other energy influences need their place in many chemical reactions.

Think about the system to apply this as a final logic coefficient. For the example case of ball milling, consider energy for when the particles collide. Particles can fracture, break into smaller particles, or react to form new particles.

Since the particle could fracture or break. Think of fractures as storing energy, until some critical amount of energy leads to a moment when the particle shatters. This is a step function. However, more than one logic step like in the previous arctangent selection is desired. Particles that have broken need a possibility to continue with size reduction. This staircase type of function can be built as shown in Equation (3.28).

$$R_{i_{dep}} = \frac{1}{2} + \frac{\arctan(W_i(R_{i_{crit}} - R_i))}{\pi} \tag{3.27}$$

$$\frac{\partial R_i}{\partial t} = \left(\frac{dE_i(t)}{dt}\frac{n_i!!}{(n_i-1)!!}\right)\ln(B_i)\,R_i\sin^{n_i}(\pi E_i(t)) \tag{3.28}$$

To understand the parameters: $E_i(t)$ is the time-dependent function for when particles break (thus it relates to energy input required to break a particle); B_i is the amount left after each break (i.e. $\frac{2}{3}$ would mean each break would leave the particles at a size of $\frac{2}{3}$ their current value); R_i is a size factor; and n_i is the width, which must be even and greater than zero, just as W_i for arctangent, the limit as $n_i \to \infty$ will make the transitions instantaneous (vertical steps), and lower values represent relaxed transitions. Next, look closer at these functions.

The integral of an even powered sine function gives a function plus a sum of sine functions with increasing frequencies and decreasing coefficients. Note, the coefficient in front of the first term is $\frac{(n_i-1)!!}{n_i!!}$ that integration by parts lowering the sine function power by two at a time creates. For example, $n_i = 6 \implies \frac{(6-1)(4-1)(2-1)}{(6)(4)(2)} = \frac{5}{16}$. Evaluate at one-half of a period ($E_i(t)$), all the sine terms contribute nothing, so $\left(\frac{dE_i}{dt}\right)^{-1}\frac{(n_i-1)!!}{n_i!!}$ is the contribution to each step, where

$\left(\frac{dE_i}{dt}\right)^{-1}$ comes from anticipating a substitution needed for the reverse chain rule to work. The lowest frequency term in the sine sum is twice that of the original. For this reason $E_i(t)$ sets the period for breaking events.

To summarize, the sine functions are the reason for a staircase. The change in each step is $\left(\frac{dE_i}{dt}\right)^{-1} \frac{(n_i-1)!!}{n_i!!}$–invert this to normalize each step as unity. Then, control the change by some fraction of the current size factor (ln$(B_i)R_i$). This allows a coupling of energy to a physical parameter. Together, they impact the probability of a reaction by the sigmoid logic function of choice. Now, all major parameters are coupled into one model: reactivity, thermodynamic and kinetic factors; solid state availability to react, currently as an effective reaction area; and energy.

Energy Dependent Terms in the Chemical Kinetics Model Equations

$$\frac{\partial Fe}{\partial t} = -R_{Fe_{dep}} R_{S_{dep}} k_{FeS} [Fe][S] \tag{3.29}$$

$$\frac{\partial Ge}{\partial t} = -R_{Ge_{dep}} R_{S_{dep}} k_{GeS_2} [Ge][S]^2 \tag{3.30}$$

$$\begin{aligned}\frac{\partial S}{\partial t} &= -R_{Fe_{dep}} R_{S_{dep}} k_{FeS} [Fe][S] \\ &\quad - 2R_{Ge_{dep}} R_{S_{dep}} k_{GeS_2} [Ge][S]^2\end{aligned} \tag{3.31}$$

$$\begin{aligned}\frac{\partial FeS}{\partial t} &= R_{Fe_{dep}} R_{S_{dep}} k_{FeS} [Fe][S] \\ &\quad - 2R_{FeS_{dep}} R_{GeS_{2dep}} k_{Fe_2GeS_4} [FeS]^2 [GeS_2]\end{aligned} \tag{3.32}$$

$$\frac{\partial GeS_2}{\partial t} = R_{Ge_{dep}} R_{S_{dep}} k_{GeS_2} [Ge][S] - R_{FeS_{dep}} R_{GeS_{2dep}} k_{Fe_2GeS_4} [FeS]^2 [GeS_2] \quad (3.33)$$

$$\frac{\partial Fe_2GeS_4}{\partial t} = R_{FeS_{dep}} R_{GeS_{2dep}} k_{Fe_2GeS_4} [FeS]^2 [GeS_2] \quad (3.34)$$

3.3 Model Understanding Examples

For some visual clarity, it may help to look at some graphs with various input parameters as the model evolves. First, look at inputs connected to all models, for example, the molar masses (Table 3.1). All models used the initial conditions where the beginning number of moles for each molecule was calculated such that there would be a stoichiometrically sufficient amount based on producing five grams of Fe_2GeS_4 from Iron, Germanium, and Sulfur. No Iron Sulfide, Germanium Sulfide, or Fe_2GeS_4 were initially present. Also, the jar use for milling is considered to be the volume of the system (50 mL).

Molecule	Molar Mass (g/mol)
Fe	55.8450
Ge	72.6400
S	32.0650
FeS	87.9100
GeS_2	136.7700
Fe_2GeS_4	312.5900

Table 3.1: Compound Molar Masses

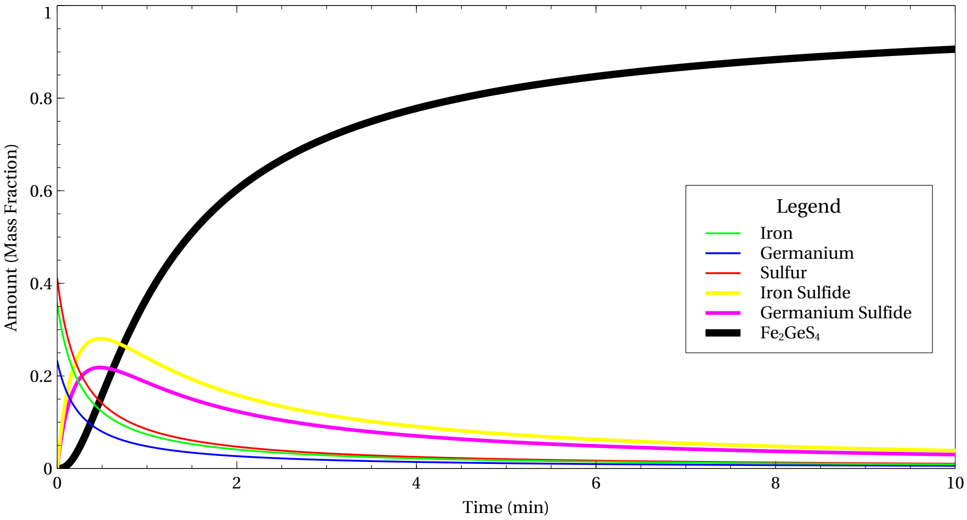

(a) Interaction Model–conservation of mass is observed along with the series of reactions.

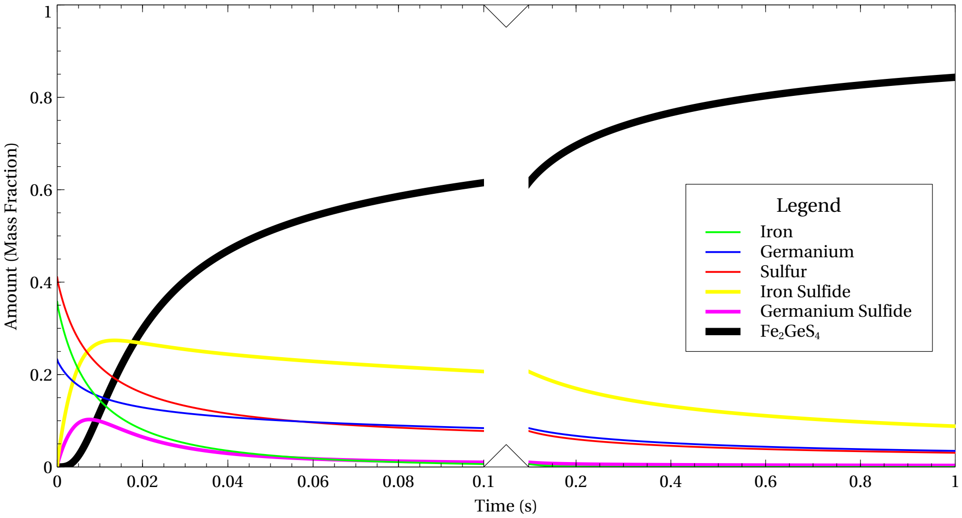

(b) Chemical Kinetics Model–with the addition of probabilities and reaction rates, the reactions now proceed at various orders.

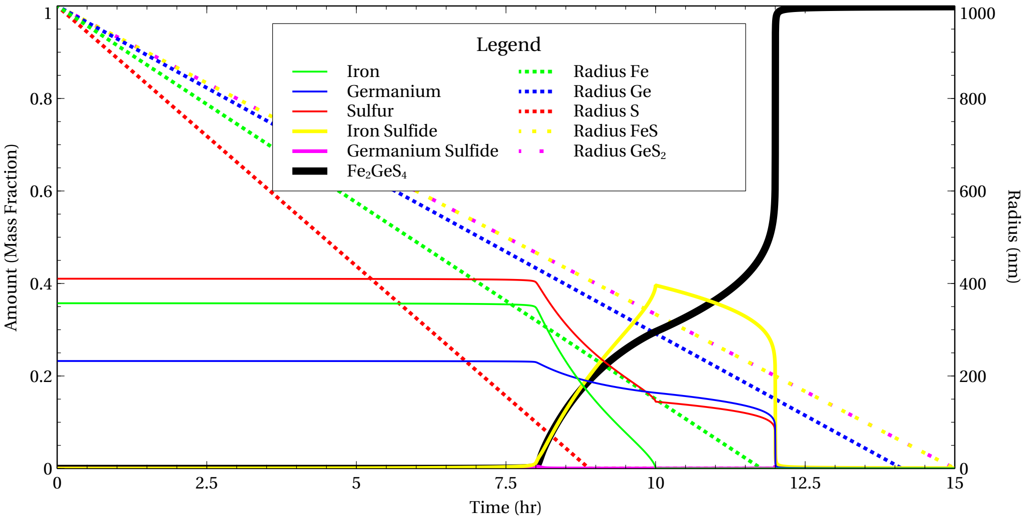

(c) Effective Reaction Area Terms in the Chemical Kinetics Model–this term has introduced size dependence ($R_{i_{crit}}$) into the reaction rates.

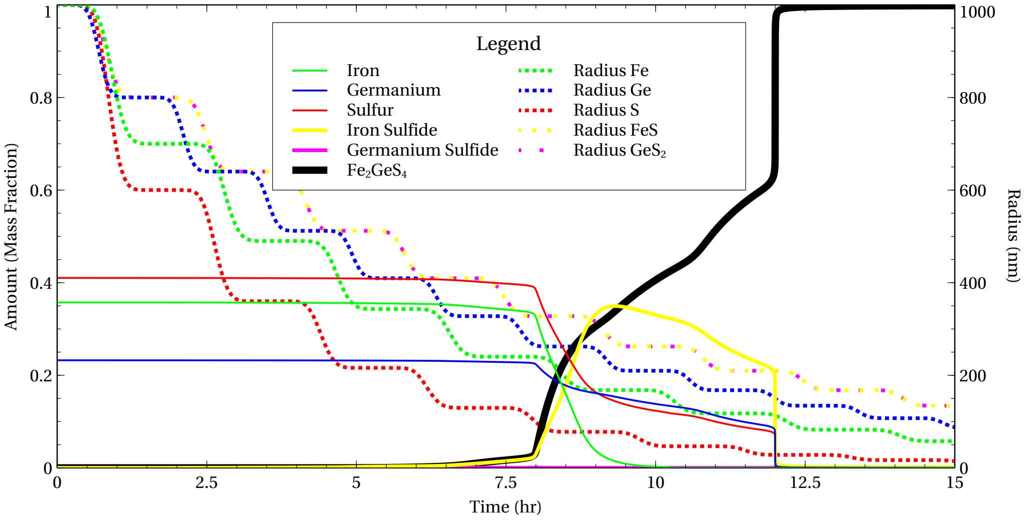

(d) Energy Dependent Terms in the Chemical Kinetics Model–the size reduction can now be controlled with an energy term ($E_i(t)$) to relate the model to ball milling.

Graph 3.1: Example graphs for understanding the model.

3.3.1 Interaction Model: Graph 3.1a

The volume is not yet considered in the interaction model, so the time for the reaction time depends solely on the amount of desired product. Most of the five grams of material will become final product after ten minutes. The most important part to note at this point is the similar curves. All of the base elements reduce exponentially. The binary compounds increase for a while and then also decrease with some exponential degree. The ternary compound follows a sigmoid shaped production.

3.3.2 Chemical Kinetics Model: Graph 3.1b

The chemical kinetics model introduced using concentration. So the initial moles were divided by the system volume and used as initial starting concentrations. Though it might be better to define an effective concentration as in some models [41], this is a demonstration model focusing on simplicity. Also, similar results can be realized with the size dependence parameters. The rate coefficients were chosen to put most of the reaction in a time of less than one second. This is a reaction that should be explosive under the proper gas conditions, so the reaction should be achievable in a short time period. The enthalpy of formation order (Fe_2GeS_4 >FeS>GeS) is also used partly as the logic in selecting rate constants, along with the observed formation order in X-Ray diffraction phase identification performed on a temporal basis [33]. Therefore, 100 $\mathrm{Lmol^{-1}s^{-1}}$ was used for K_{FeS}, 50 $\mathrm{L^2mol^{-2}s^{-1}}$ for K_{GeS_2}, and 1000 $\mathrm{L^2mol^{-2}s^{-1}}$ for $K_{Fe_2GeS_4}$. Again, these numbers should be measured experimentally, but the purpose here is a demonstration. Most of the five grams of material will become final product after one second, the most important part to note is now the varying curves. All of the base elements follow different degrees of reducing exponentially. Sulfur having the highest degree and Germanium the lowest. This is expected, due to the order of the reactions and their temporal formation order. The binary compounds increase for a while and then also decrease with different exponential degrees, as they are also of different reaction orders. Finally, all of this information is absorbed into the degree with which the final product can be produced, as it depends on all reactions. The graph is asymmetrically presented to show that the induction period and the inflection point, where it switches to asymptotic behavior, all happens in less than two-hundredths of a second.

3.3.3 Effective Reaction Area Terms in the Chemical Kinetics Model: Graph 3.1c

With effective reaction area dependence, set a size-related parameter for which the reaction will occur. Here was used an initial size of one micron and a critical size of 100-200 nanometers for $R_{i_{crit}}$ (Table 3.2). As there were formations of particles in a range from 20-200+ nanometres seen in the milling synthesis, as well as from the paper by Park et al. [33], this should be reasonable. The slope of R (k_{i_R}) was set to make the reaction start around eight hours finish at twelve hours (Table 3.3). The width (W) was set to make an early appearance of Iron Sulfide sometime after four hours, and of an easily noticeable amount around ten hours. Also, keeping Germanium Sulfide from showing and having a reasonable amount of the ternary compound by ten hours were set with the widths (Table 3.4). These parameters were also chosen to match with X-Ray diffraction phase identification performed on a temporal basis [33].

$R_{i_{crit}}$	Critical Size (nm)
$R_{Fe_{crit}}$	150.0
$R_{Ge_{crit}}$	150.0
$R_{S_{crit}}$	100.0
$R_{FeS_{crit}}$	200.0
$R_{GeS_{2crit}}$	200.0

Table 3.2: Reaction Critical Size

k_{i_R}	Slope (nm/s)
k_{Fe_R}	$-(1000.0 - R_{Fe_{crit}})/(10.0 \times 3600)$
k_{Ge_R}	$-(1000.0 - R_{Ge_{crit}})/(12.0 \times 3600)$
k_{S_R}	$-(1000.0 - R_{S_{crit}})/(8.0 \times 3600)$
k_{FeS_R}	$-(1000.0 - R_{FeS_{crit}})/(12.0 \times 3600)$
$k_{GeS_{2R}}$	$-(1000.0 - R_{GeS_{2crit}})/(12.0 \times 3600)$

Table 3.3: Size Factor Slope

W_i	Width (rad/m)
W_{Fe}	1000.00
W_{Ge}	1000.00
W_S	0.50
W_{FeS}	0.01
W_{GeS}	0.01

Table 3.4: Reaction Arctangent Width

3.3.4 Energy Dependent Terms in the Chemical Kinetics Model: Graph 3.1d

Similar to how size dependence has been set, the energy parameters are also mostly a proof of principle demonstration since there has not been enough appropriate data collected for good statistical matching. The breaking fraction (B_i) was set based on material hardness, such that softer materials break more (Table 3.5). The step width (n_i) was set to ten for a relaxed parameter. Finally, timespan for the steps was set with a breaking energy time ($E_i(t)$) as a linear function of time with a coefficient for maintaining the same time as the size factor slope, k_{i_R} (Table 3.6). Each coefficient comes from an analytical solution of the size factor functions, R_i, which have a rate of change dependent on their own value; therefore, the natural logarithm appears. Yet, again one can see that with a little effort temporal matching is quick and simple.

$E_i(t)$	Energy Function
$E_{Fe}(t)$	$\frac{\ln(R_{Fe_{crit}}/1000.0)}{10.0\times3600\ln(B_{Fe})}t$
$E_{Ge}(t)$	$\frac{\ln(R_{Ge_{crit}}/1000.0)}{12.0\times3600\ln(B_{Ge})}t$
$E_S(t)$	$\frac{\ln(R_{S_{crit}}/1000.0)}{8.0\times3600\ln(B_S)}t$
$E_{FeS}(t)$	$\frac{\ln(R_{FeS_{crit}}/1000.0)}{12.0\times3600\ln(B_{FeS})}t$
$E_{GeS}(t)$	$\frac{\ln(R_{GeS_{2crit}}/1000.0)}{12.0\times3600\ln(B_{GeS})}t$

Table 3.5: Breaking Fraction

B_i	Fraction
B_{Fe}	0.70
B_{Ge}	0.80
B_S	0.60
B_{FeS}	0.80
B_{GeS}	0.80

Table 3.6: Breaking Fraction

3.4 Model Application Example

With the basic outline in place, any reaction can be fit given the appropriate data. Fitting parameters such as the various logical widths and inflection points (critical parameters) yield information on the system behavior. For example, as to how mechanical and chemical interactions lead to a ternary compound (Fe_2GeS_4) synthesis during ball milling. Where do the major dependencies of the reaction lay? Mechanically induced self-propagating reactions (MSR), such as the aforementioned ternary compound's formation, follow many interlinked processes [43]. These processes can be categorized to energy, interactions, and morphology for elements in the system [40].

As all of these categories have already been placed in the model, all that remains is building an example. Looking at the examples for understanding, Section 3.3, nothing in the chemical kinetics should change. So, to expand more on the model's flexibility, a demonstration will be made using formation (F_{ij}) and agglomeration (A_i), as well as size dependent breaking ($B_i(R_i)$), and non-linear energy dependence ($E_i(t)$). The result can be viewed in Graph 3.2.

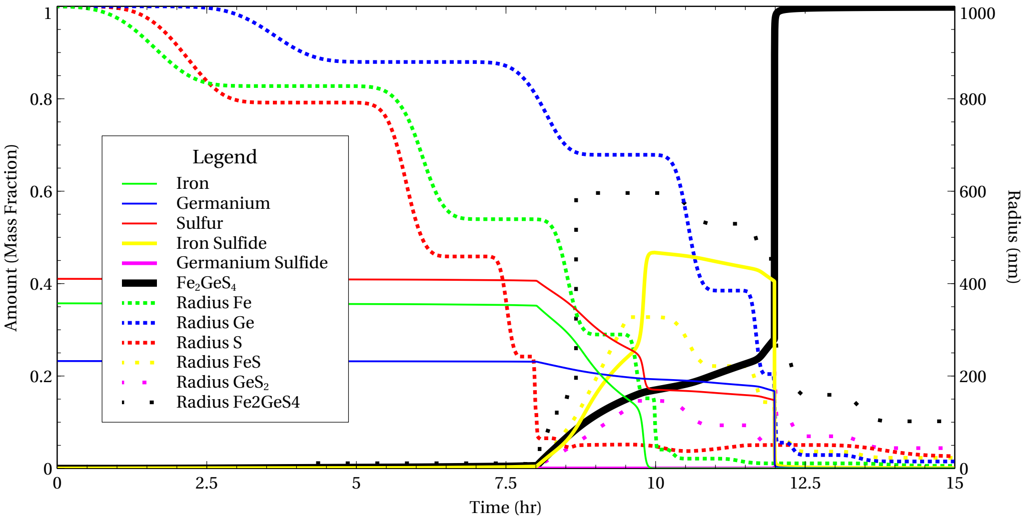

Graph 3.2: Application of the Model–the effects of formation, agglomeration, size dependent breaking, and non-linear energy dependence are all quite apparent in the changing effective reaction area terms represented by varying radii of the elements and compounds.

Model Application Equations

$$B_i(R_i) = \frac{(1 + 2\arctan(W_{i_B}(R_i - R_{B_{crit}}))}{2\pi} \times (B_{i_{min}} - B_{i_{max}}) + B_{i_{max}} \tag{3.35}$$

$$E_i(t) = \sqrt[3]{W_{i_E}(t - t_{i_{crit}})} \tag{3.36}$$

$$A_i = \frac{(1+2\arctan(W_{i_A}(R_{A_{crit}} - R_i))}{2\pi}\left([i]\frac{M_i}{D_i}\right)^2 R_i \tag{3.37}$$

$$R_{form_{ij}} = \sqrt[a]{R_i^a \frac{D_i}{D_{ij}} + R_j^a \frac{D_j}{D_{ij}}} \tag{3.38}$$

$$R_{form_{ijmax}} = \frac{(1+2\arctan(W_{HVY}(R_{form_{ij}} - R_{ij}))}{2\pi} \tag{3.39}$$

$$[i]_{exist} = \frac{(1+2\arctan(W_{HVY}([i] - X_i[Fe_2GeS_4]_{final}))}{2\pi} \tag{3.40}$$

$$F_{ij} = [i]_{exist}[j]_{exist}R_{form_{ij}}R_{form_{ijmax}}R_{ij_{dep}}k_{ij} \tag{3.41}$$

$$R_{i_{dep}} = \frac{1}{2} + \frac{\tan^{-1}(W_i(R_{i_{crit}} - R_i))}{\pi} \tag{3.42}$$

$$\begin{aligned}\frac{dR_i}{dt} &= [i]_{exist}A_i \\ &+ \left(\frac{dE_i(t)}{dt}\frac{n_i!!}{(n_i-1)!!}\right)\ln(B_i)\,R_i\sin^{n_i}(\pi E_i(t))\end{aligned} \tag{3.43}$$

$$\begin{aligned}\frac{dR_{ij}}{dt} &= [ij]_{exist}A_{ij} + [ij]_{exist}F_{ij} \\ &+ \left(\frac{dE_{ij}(t)}{dt}\frac{n_{ij}!!}{(n_{ij}-1)!!}\right)\ln\left(B_{ij}\right)R_{ij}\sin^{n_{ij}}\left(\pi E_{ij}(t)\right)\end{aligned} \tag{3.44}$$

$$\frac{dFe}{dt} = -R_{Fe_{dep}}R_{S_{dep}}k_{FeS}[Fe][S] \tag{3.45}$$

$$\frac{dGe}{dt} = -R_{Ge_{dep}}R_{S_{dep}}k_{GeS_2}[Ge][S]^2 \tag{3.46}$$

$$\begin{aligned}\frac{dS}{dt} &= -R_{Fe_{dep}} R_{S_{dep}} k_{FeS} [Fe][S] \\ &\quad - 2 R_{Ge_{dep}} R_{S_{dep}} k_{GeS_2} [Ge][S]^2\end{aligned} \tag{3.47}$$

$$\begin{aligned}\frac{dFeS}{dt} &= R_{Fe_{dep}} R_{S_{dep}} k_{FeS} [Fe][S] \\ &\quad - 2 R_{FeS_{dep}} R_{GeS_{2dep}} k_{Fe_2GeS_4} [FeS]^2 [GeS_2]\end{aligned} \tag{3.48}$$

$$\begin{aligned}\frac{dGeS_2}{dt} &= R_{Ge_{dep}} R_{S_{dep}} k_{GeS_2} [Ge][S] \\ &\quad - R_{FeS_{dep}} R_{GeS_{2dep}} k_{Fe_2GeS_4} [FeS]^2 [GeS_2]\end{aligned} \tag{3.49}$$

$$\frac{dFe_2GeS_4}{dt} = R_{FeS_{dep}} R_{GeS_{2dep}} k_{Fe_2GeS_4} [FeS]^2 [GeS_2] \tag{3.50}$$

3.4.1 Formation Term in the Application Model

To understand how the formation of new particles from the reactions of other elements in the system have been modeled, look at each term of Equation (3.41). Many of the terms are conditional and/or weighted logic.

The test of element existence ($[i]_{exist}$) could be written as a Heaviside function; however, using arctangent with a large width (W_{HVY}) keeps the equation continuous and more flexible. Also, using a difference, instead of just the element in question allows the setting of an effective zero. That is to say, zero can become proportional to the amount of stuff involved in the reaction. Using some fraction (X_i) of the final amount of product ($[Fe_2GeS_4]_{final}$) allows such an approach. Thus, formation of new particles relies on existence of the elements required to produce the new compound.

The largest possible new formation ($R_{form_{ijmax}}$) would be two particles coming together and reacting to form a new particle of weighted size ($R_{form_{ij}}$) from its constituent parts. So, the elements are weighted against their current density (D_i and D_j) to that of the new compound density (D_{ij}). The size growth rate and densities used depends on the particle dimensions (a), such that one could use 1-D, 2-D, or 3-D growth. In this application, $a = 3$, and the growth is by volume. As formation should not lead to growing larger than this weighted size, a logical cap is put in place ($R_{form_{ijmax}}$).

Finally, the formation is in proportioned to the maximum, based on the rate with which the chemical reaction is proceeding ($R_{ijdep}k_{ij}$). This way, the formation does not occur just because the constituents for a given product are present, the formation rate depends as well on the reaction probabilities.

3.4.2 Agglomeration Term in the Application Model

Particles colliding with themselves can lead to agglomeration. The interaction probability is calculated as a volume ratio product and the amount is set by a logic curve based on a critical size.

To represent the physical collisions of particles and not the individual elements, a volume ratio is calculated using the concentration value, molar mass, and density ($[i]\frac{M_i}{D_i}$). This is the ratio of volume to a given reactant or product out of the system volume. Thus, the probability of self-interaction is taken as a product of each ratio. The assumption is that it represents the probability of finding the element and probabilities are equal everywhere.

The logic curve is to account for variance in agglomeration based on size. In general, as the particles get smaller more agglomeration is observed. Also, above a critical size ($R_{A_{crit}}$) nothing mentionable is observed. Therefore, the smallness at which particles start to agglomerate can be set as well as how relaxed the action is to this parameter by the width (Wi_A). Again, arctangent has been chosen for the logic function, but any sigmoid logic would work.

Finally, the growth is in proportion to current size (R_i). That way, at most, two particles can make a size proportional to their total sum. A look at formation reveals this as the same logic seen in Equation (3.38). As each density would be the same, $\sqrt[a]{2}$ is the only factor left out. This has been done intentionally since R is an effective reaction area to be decided based off observable data. Thus, differential equation proportionality order is maintained, and the constant can be absorbed into the logic function.

3.4.3 Size Dependent Breaking Term in the Application Model

The breaking functions for ball milling are quite abundant. In order to break a crystal, bond layers must be pulled apart past their elastic limit [44]. Since energy stored from material strains is around dislocations, corners, and such; and therefore, not uniformly distributed, breaking can be quite unpredictable.

Therefore, to capture prevalent trends, think of the impacts in a mill (or any collision). The contact point of an applied force is at the surface and then the mechanical energy can propagate through the material by various means such as deformations, vibrations, heat, etc. Since the available surface (contact area) and the volume (energy storage zone for fractures) change in ratio as the particle reduces in size, so does the relative size of a crack of given depth from an impact.

Using this logic, breaking fractions vary from a minimum ($B_{i_{min}}$) to maximum ($B_{i_{max}}$) amount as the particles reduce in size. Again this logical curve has an inflection size ($R_{B_{crit}}$) about which the minimum and maximum break fractions are centered. There is also a width (W_{i_B}) to account for how sharp the change occurs between the two amounts.

3.4.4 Non-linear Energy Term in the Application Model

For much of the same reasons used in determining the breaking, the energy between breaks varies with milling time. Collisions not only break materials, but also, store energy and cause dislocations.

As milling continues, a particle decreases in size. Surface area and dislocations increase, energy storage locations; however, the overall available space, volume, for energy to store decreases. At some point, the size becomes small enough that the particles flow like a fluid and the glancing collisions lead to less breaking. For describing this increase and decrease, a monotonically decreasing function with an increasingly negative slope that reaches and inflection where the slope begins decreasing is chosen.

By using a cube root function, the time for when an inflection occurs is selected ($t_{i_{crit}}$) just as other critical parameters have been selected for logic functions. There is also a width (W_{i_e}) to control the breadth of the change. Thus, over the timespan for experiment, the time between breaks is seen to decrease and then increase in Graph 3.2.

Chapter 4

Absorber Synthesis

Previous syntheses have been done using tube furnaces, solution syntheses, and ball milling methods. In an effort to keep with green synthesis procedures, ball milling was the synthesis choice for this experiment.

4.1 Ball Milling Synthesis

Prior to material loading for ball milling synthesis, a premixture of dry elements was prepared via mortar and pestle. Then, various milling parameters were varied in multiple mechanochemical syntheses using the ball milling machine.

4.1.1 Mortar and Pestle Premixture

Standard wash procedures were used to prepare the mortar and pestle.

1. Wash the agate mortar and pestle with soap and water and leave in the air to dry.

   This step is to remove bulk debris from the surface of the agate.

2. Wipe the mortar and pestle with acetone and leave in the air to dry.

   This step is to remove materials that are insoluble in water from the surface.

Figure 4.1: Mortar and pestle premixing

3. Rinse the mortar and pestle with methanol and leave in the air to dry.

   This step is to remove the acetone.

4. Rinse the mortar and pestle with deionized water and leave in the air to dry.

   This step is to remove the methanol.

Following the preexisting literature by Park et al. [33], measures were taken to prepare a premixture of the elements iron (Fe), germanium (Ge), and sulfur (S) in a ratio of 2 : 1.5 : 4 in order to synthesize Fe_2GeS_4.

First, a bulk crystal of pure germanium was ground into powder using the clean mortar and pestle. The powder was then transferred into a jar for storage and the mortar and pestle cleaned according to the previously outline steps.

To prepare approximately 20 grams of premix, some of the germanium powder, along with iron powder, and sulfur crystals were all mixed, in a ratio of 2 : 1.5 : 4, using the clean mortar and pestle as seen in Figure 4.1. Upon visually reaching a feed size of submillimeter for the powder, the premix was transferred into a jar for storage.

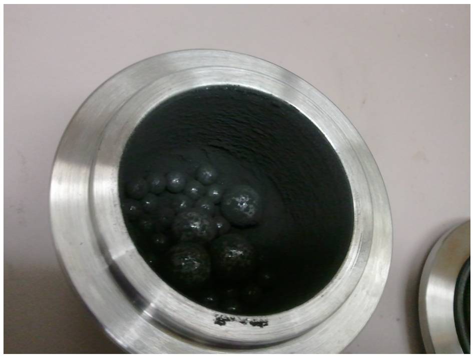

Figure 4.2: The final product

4.1.2 Ball Milling

Using 5 : 8 scaling, due to using a 50 milliliter jar in comparison to the 80-milliliter jar used by Park et al. [33], previously used mass ratios of milling balls and premix were maintained for the first synthesis. After following jar checking procedures, the premix was left to mill for 12 hours continuously. Characterization later revealed the reaction as a success.

For the first run, approximately 16 grams of 10-millimeter and 16 grams of 5-millimeter Zirconium Oxide balls were used in a 50-milliliter capacity steel jar. Approximately 3.2 grams of premix was added to the steel jar with the Zirconium Oxide balls. A counterbalance using a 50-milliliter capacity steel jar with approximately 24 grams of steel balls was also prepared for use in a Retsch PM 200 planetary ball mill.

The planetary ball mill was set up with the rotation speed setting at 550 revolutions per minute. Following the manual for long milling operations, jar clamps and security were checked at 3 minutes, 1.05 hours, and 3.9 hours prior to running the mill continually for 12 hours. The final product was a matte grey-black as seen in Figure 4.2.

Subsequent milling runs varied the milling time, rotation directions changing at various intervals, and the milling ball to premix weight ratios. Using 30 minute rotation direction change intervals seemed to significantly cut down on agglomeration deposits of the powder to the side walls of the milling jar. It was also found that the reaction would reach completion even if milling was halted for large intervals. For example, one run milled for 7 hours and then halted for approximately 13.5 hours before finishing the synthesis with 5 more hours of milling time.

Further plans for using the ball mill were halted due to a safety slider needing repair work. Thus, synthesis was never completed using electronic grade purity elements. Also, final fineness was lacking in uniformity. This was likely due to the mixed use of 5 and 10-millimeter diameter milling balls; however, confirming such hypothesis will need to be left for future work.

4.2 Absorber Characterization

The quickest verification of successful compound synthesis, post ball milling, is visual confirmation. When checking the product during various milling experiments, it became clear that the visual change from a metallic gray to a matte gray-black appearance was the simplest confirmation of a chemical reaction. This change is quite apparent if the material in Figure 4.1 is compared to the product seen in Figure 4.2. However, oxidation of metals is common in ball milling. Seeing as Hematite is black in appearance and is an iron oxide, some other confirmation was necessary in order to validate the final product.

4.2.1 Scanning Electron Microscopy (SEM) Characterization

One way to rule out Hematite is a closer visual inspection of the product. Discussed in Section 1.4.1, SEM is a good way to investigate size and morphology of very small materials. As Hematite crystals are in the trigonal system, hexagonal scalenohedral class, and the desired product is in the orthorhombic system, dipyramidal class, a visual distinction is easy enough by the difference in prevalent geometries. The same general observation is also true of the reactants in comparison with the final product. The change in observable geometries allows for a quick visual observation of the reaction. As can be seen in Figure 4.3 the formation of plate-like structures gives a visual signal that the reaction has commenced.

The ten thousand times magnification level images for the reaction initiation (Figure 4.3j) and the reaction near completion (Figure 4.3k) show the beginning of platelets forming and nearly all of the material in stacked plate-like geometries. The organization of Figures 4.3a, 4.3b, 4.3d to 4.3i and 5.5a is such that the same sample location is viewable at different magnifications by column and different samples are in different columns. For example: Figures 4.3a, 4.3b and 5.5a are all at one hundred times magnification, with each image as a different sample; and Figures 4.3a, 4.3d and 4.3g are all the same sample at one hundred, one thousand, and ten thousand times magnification respectively.

As stated, this is a quick visual indication. The final compound has an olivine structure and we can see the change in morphology into plate-like structures, indicating the possibility of an olivine compound. For a more accurate verification of the material, chemical composition, and phase is analyzed using XRD.

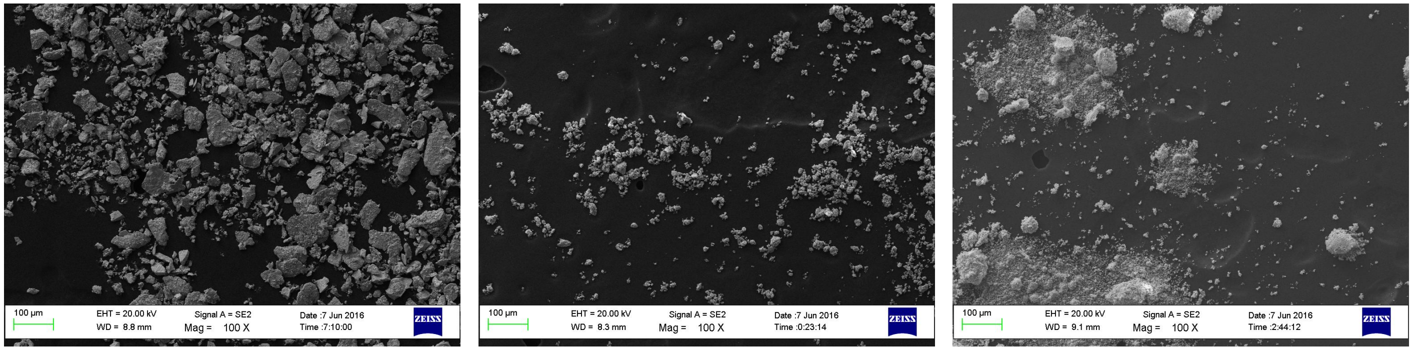

(a) The reactants at 100X **(b)** Starting to react at 100X **(c)** Near final product at 100X

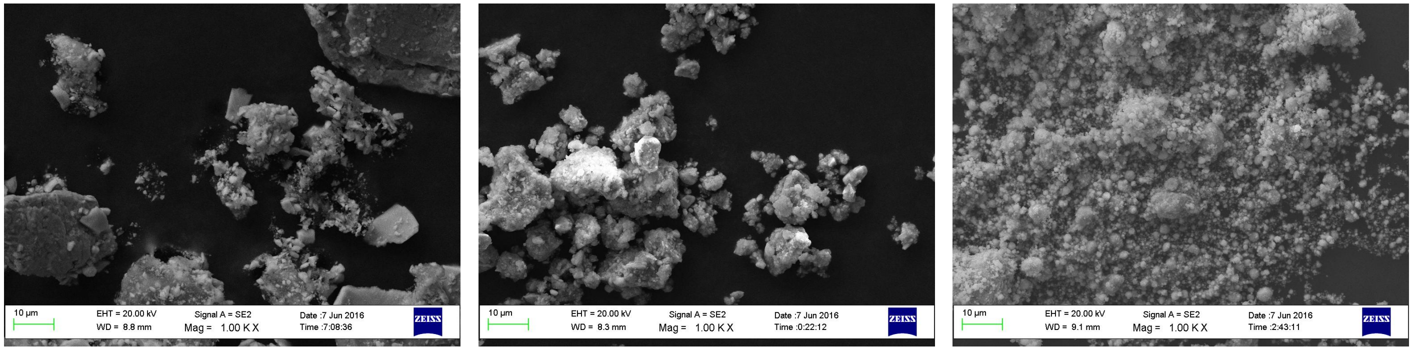

(d) The reactants at 1,000X **(e)** Starting to react at 1,000X **(f)** Near final product at 1,000X

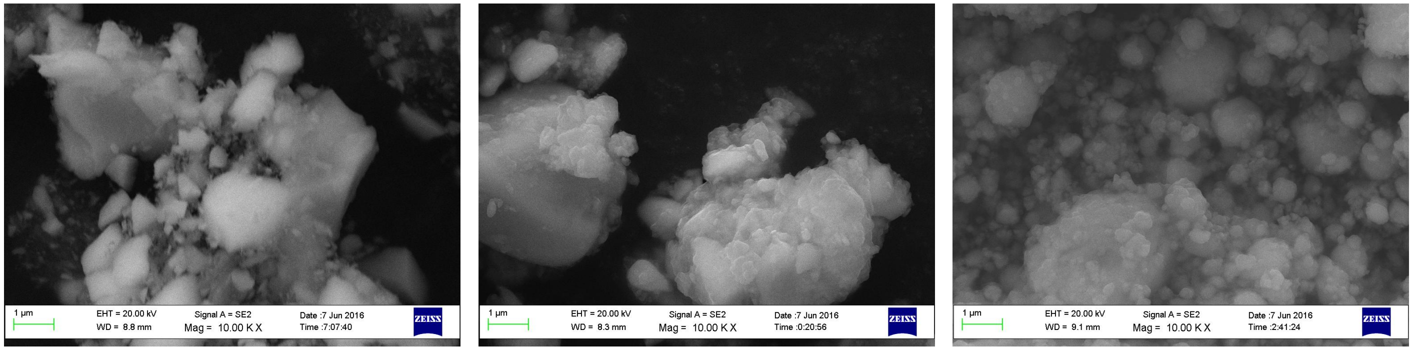

(g) The reactants at 10,000X **(h)** Starting to react at 10,000X **(i)** Near final product at 10,000X

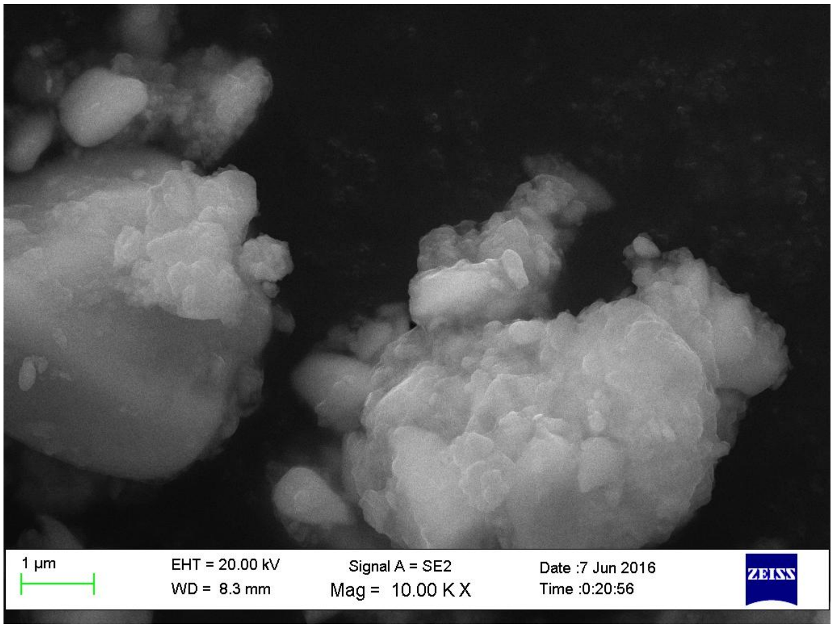

(j) Starting to react at 10,000X

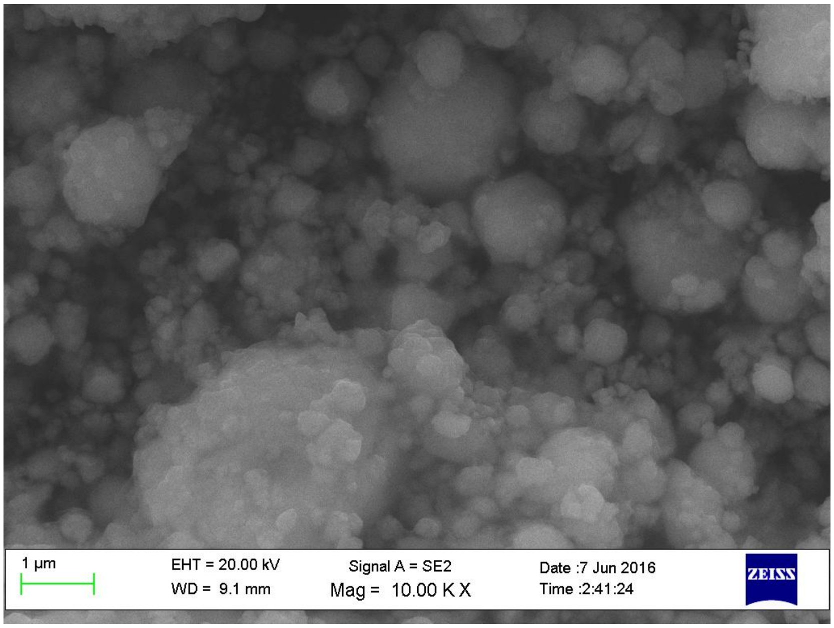

(k) Near final product at 10,000X

Figure 4.3: Visual progression of the reaction with 4.3h and 4.3i reproduced larger for better viewing of final changes during the reaction.

4.2.2 X-Ray Powder Diffraction (XRD) Characterization

Every crystal has a distinct set of constructive peaks when an X-ray scatters at various angles. The cause for this observation is briefly introduced in Section 1.4.2. A quick look at some various databases and one can visually match their samples. With the aid of computer software, which compares selected peaks with those stored in databases of the user's choice, it can be overwhelming at first. However, with some understanding of the different types of reference samples such as: theoretical versus measured; or verified as a valid reference versus unverified; the system becomes navigable. With some experience on tuning the searches and setting the peak patterns, the task becomes even more manageable.

For example, peak matching is visualized in Graph 4.1 by the color of each elements' lattice spacing reference pattern being superimposed onto the premix sample's diffraction count pattern. As almost all peaks are accounted for, the premix is fairly pure.

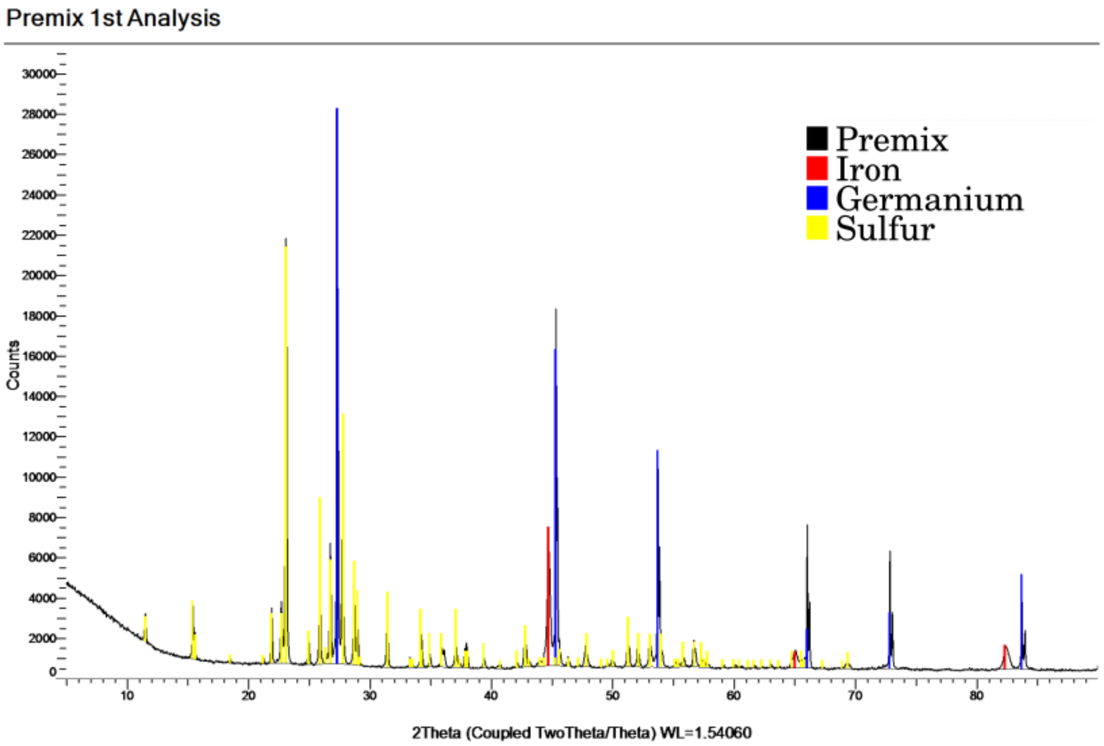

Graph 4.1: Identification of reactants via XRD analysis. Reference patterns for iron (red), germanium (blue), and sulfur (yellow) have been superimposed onto the premix's XRD pattern.

Some may find it more appealing to remove the background as has been done in Graph 4.2 in comparison with the raw pattern shown in Graph 4.1. The peaks labeled 2998, 2765, and 1798 at 2θ angles greater than 65° are not really unidentified peaks. They are most likely the $K_{\alpha 2}$ doubles of their adjoining $K_{\alpha 1}$ signal. This is discernible by their shape and relative intensity. The signals from the $K_{\alpha 2}$ radiation gives approximately half the intensity of the $K_{\alpha 1}$ and the shape of the signal is the same. These two signals are less superimposed at larger angles, and the dual peaks become more apparent. This is not the case for the peak near 36° labeled 842. This peak likely belongs to some contaminate. The impurity could be present due to the raw elements not being pure or because of contamination during the preparation of the premix.

Similarly, we can look at the XRD pattern of a nearly complete reaction and verify the chemical composition and phase of our final product. As seen in Graph 4.3, the measured pattern is a good match with the reference patterns–confirming a successful synthesis.

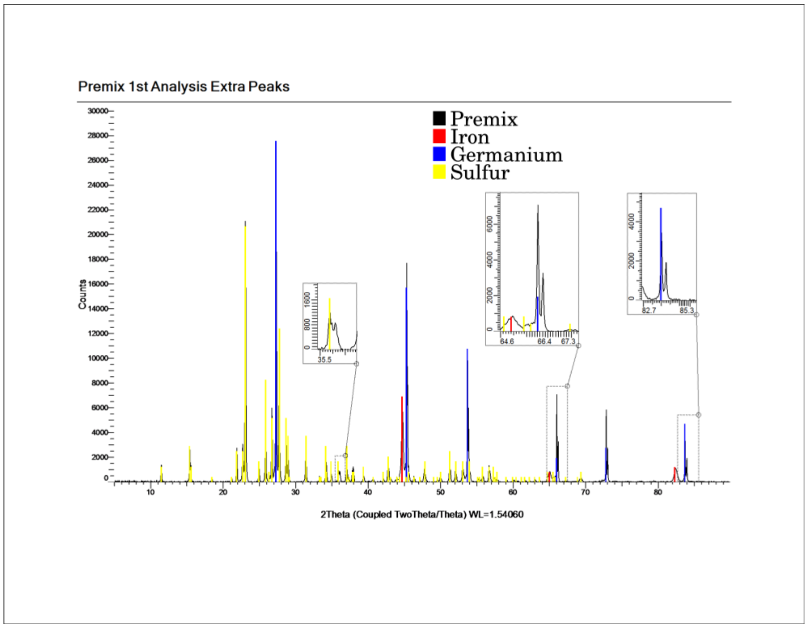

(a) Peak windowing

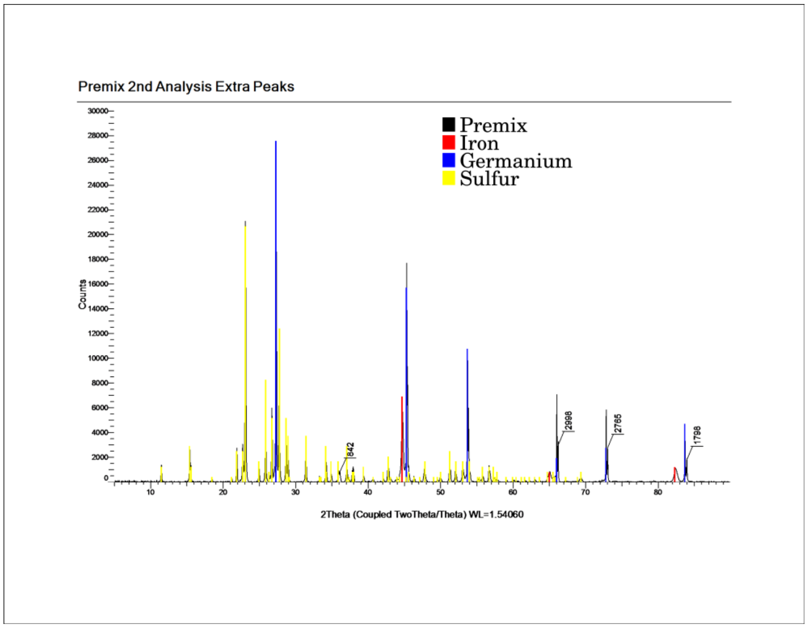

(b) Peak labeling

Graph 4.2: Peaks can be windowed as in 4.2a to help visualize them or they can be marked as done in 4.2b.

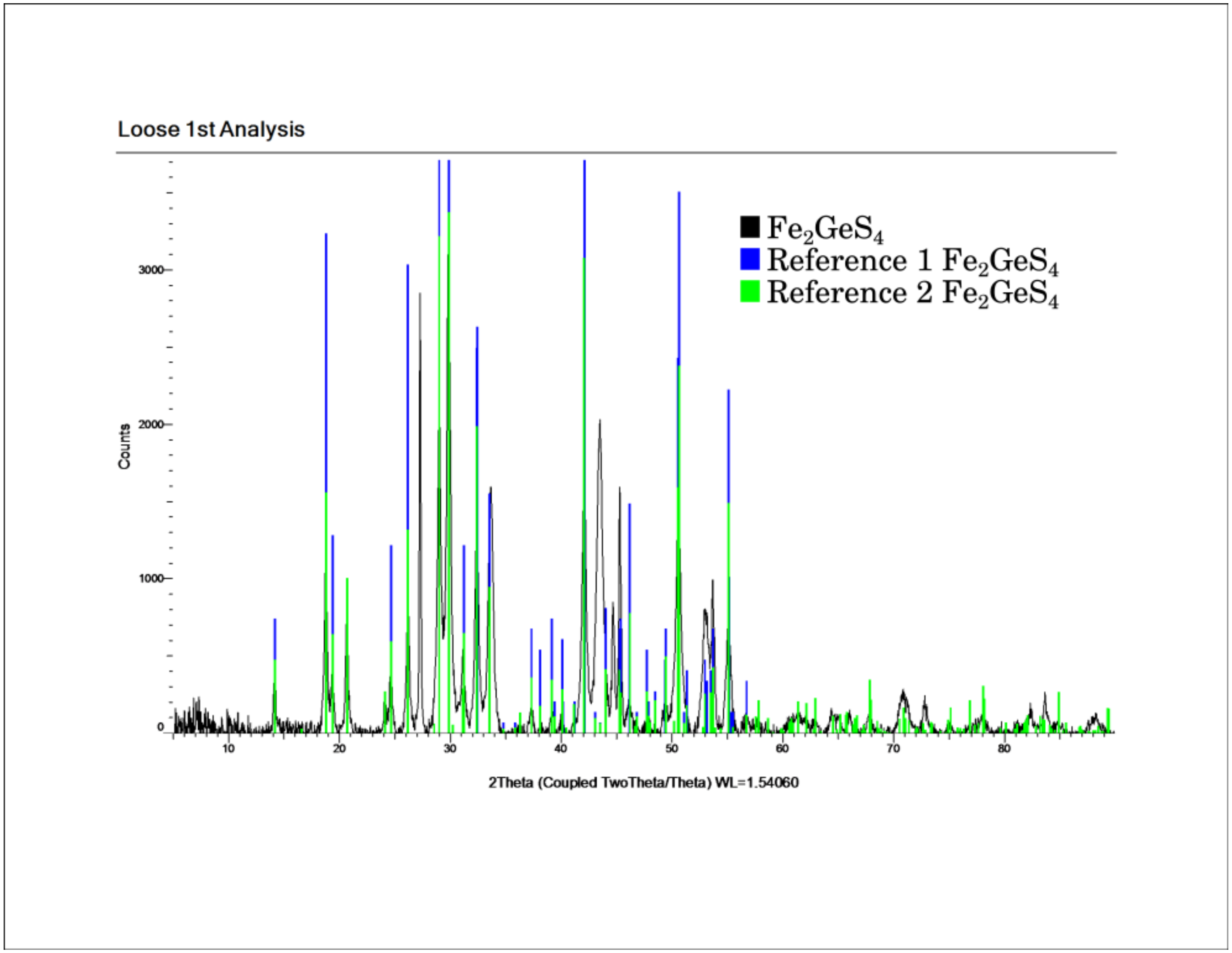

Graph 4.3: Identification of the final product via XRD analysis. Reference patterns for both a theoretical and measured XRD pattern for Fe_2GeS_4 are shown in blue and green.

The unmatched peaks in Graph 4.3 have been resolved in Graph 4.4. The reaction is revealed to be incomplete by the remaining presence of germanium. Also, a reaction path is revealed by the presence of the intermediary product, iron sulfide. Scraping the sample from the wall of the milling jar also reveals unreacted sulfur not present in the loose product. This has been made clear in Graph 4.5, where the windowed peak around 23.2° shows sulfur in the scraped sample, but not the loose sample. Such observations were useful in adjusting milling parameters to have a higher amount of reaction completeness.

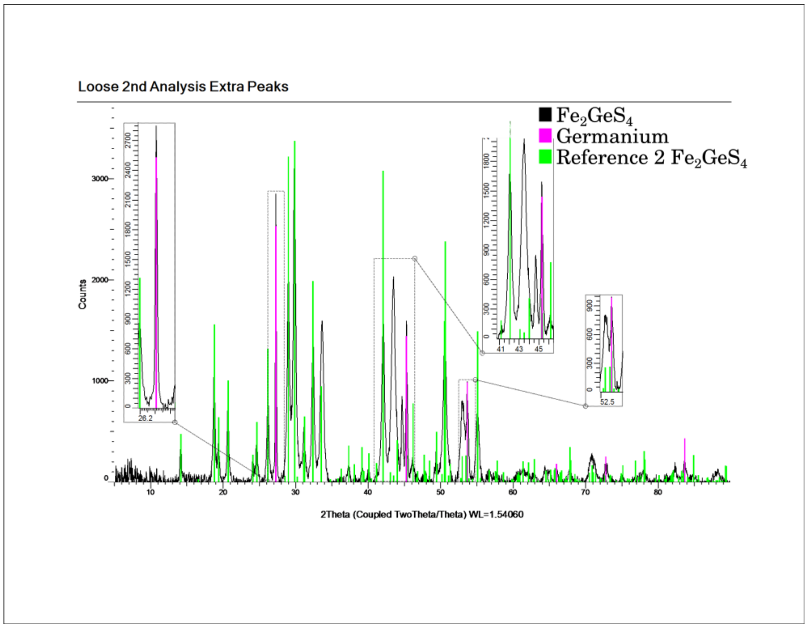

(a) Germanium (purple) peak identification

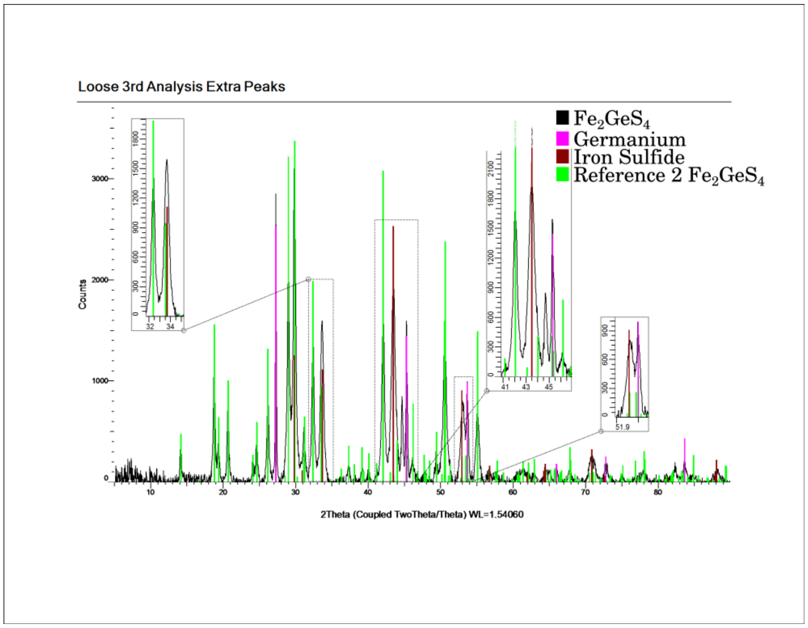

(b) Iron sulfide (reddish brown) peak identification

Graph 4.4: Unknown peaks can be windowed for easier identification. This has been done for the identification of unreacted germanium (4.4a) and intermediary product iron sulfide (4.4b).

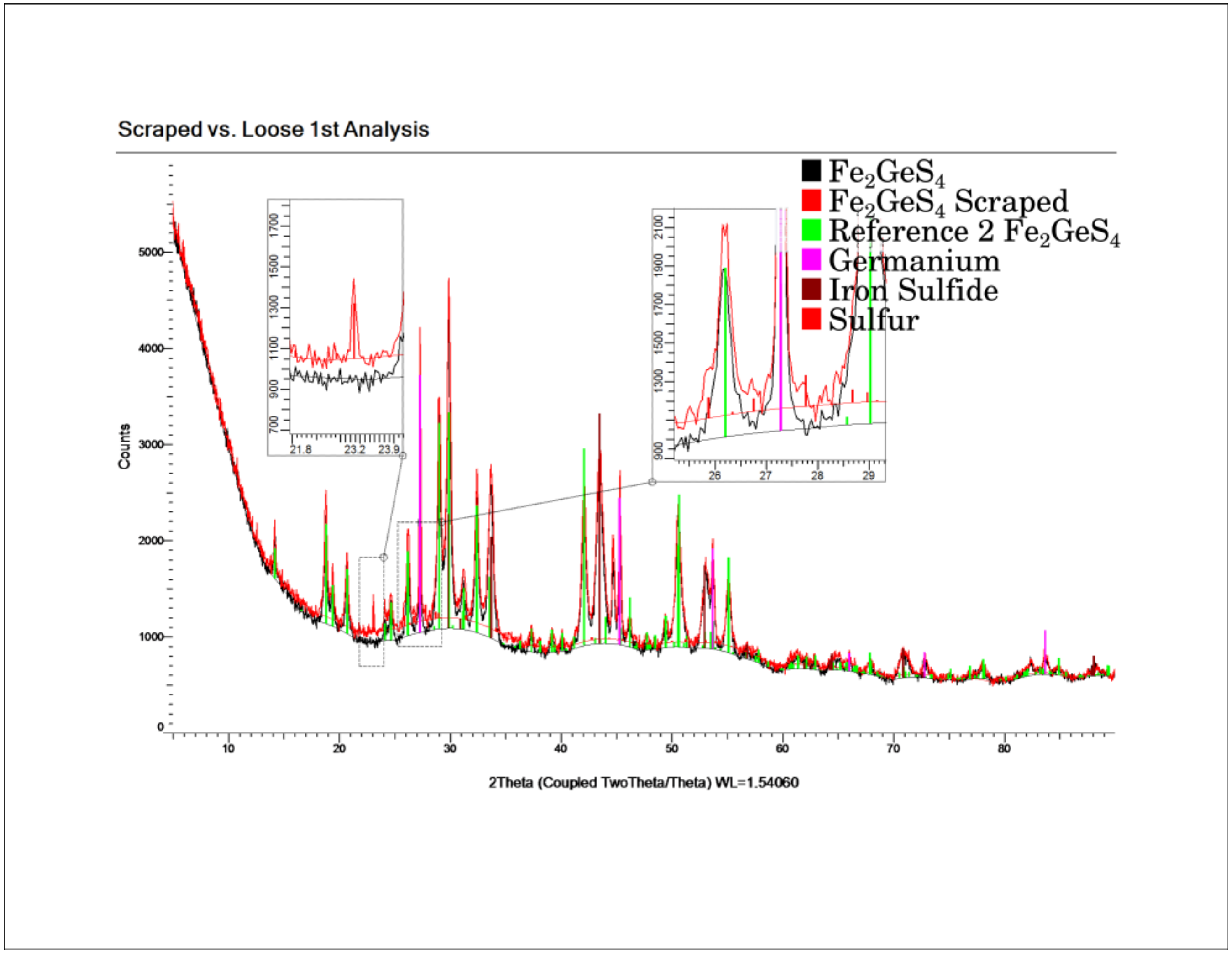

Graph 4.5: Identification of unreacted sulfur (red) in the final product via XRD analysis. Sulfur is present in the XRD pattern from the scraped sample (red) but not the loose sample (black).

Chapter 5

Thin Film Application

Many methods for thin film deposition exist and a few have been discussed in Section 1.5. By using nanoparticles synthesized via ball milling, as outlined in Chapter 4, various methods for colloid suspensions were tested and implemented in film depositions.

As the overall focus of work has an underlying theme of green energy, not all methods that are chosen necessarily correlate with those which are most commonly used. The stabilizers and solvents often used to make a liquid for suspending ceramic nanoparticles in a colloid are abundant with heavy, polar, long chain organic molecules. Many of these are toxic. So, many attempts were done with a simple suspension in water and/or ethanol. As these eventually settle, agitation is necessary, and viscosity was often not correct for spin coating thick enough layers. Thus, for many films drop casting was used.

5.1 Spin Coating

Based on the various literature, early spin coating experiments were done with high weight ratio to allow for quick visual analysis of the results. That is to say, higher weight concentrations tend to yield thicker single coat films, which made identification of issues doable by unaided sight or optical microscopy. Spin speeds and times were varied in order to see if an optimum combination was possible. Various papers have similar explanations of spin speed and spin time. For example, Zhao and Marshall [45] show a nonlinear decrease of thickness with relation to time, and Tyona [46] shows a nonlinear decrease of thickness with relation to spin speed.

With this in mind, extremes were tested to see various impacts on the final film. A major factor in determining the thickness is initially set by the amount of spin-off material, which leaves the substrate as waste. Thus, some initial films would spin for only one or two seconds at a given speed (2,000 rpm for example) before slowing down for evaporation of remaining liquid (1,000 rpm for example). This lead to a clear understanding of acceleration and speed choices for films. It was realized that for water or ethanol suspensions, acceleration values which were too low lead to nonuniform films, and speed values that were above 3000 rpm made little difference in making the films any thinner. Somewhere around 5,000-7,000 rpm, thicker films would start to break. Though various weights were tested, no uniform, continuous, single coat films could be made at speeds above 500rpm. As observed by Wang et al. [47], speeds that are too high result in a sparse dispersion of the nanoparticles. However, lowering the speed below 300 leads to no waste spin-off. Thus, continuous, uniform films could be obtained at around 200 rpm, but this only leads to a slight improvement in film uniformity and nanoparticle organization in comparison with a drop cast.

With a basic understanding to some of the limitations for spin coating the nanoparticles, various measures were taken to improve the suspension. A comparison of a simple drop cast of the unsettled solution versus some separation of nanoparticles after settling revealed a path to improving film quality. As can be seen in Figure 5.1, simply leaving the suspension for some time after agitation and pulling off the remaining unsettle suspension after some time can greatly reduce the presence of larger particles. During slower spin coats these larger particles cause agglomerations that disrupt the film uniformity. At higher speeds, the larger particles tend to be drawn off the substrate causing comet streaks in the film.

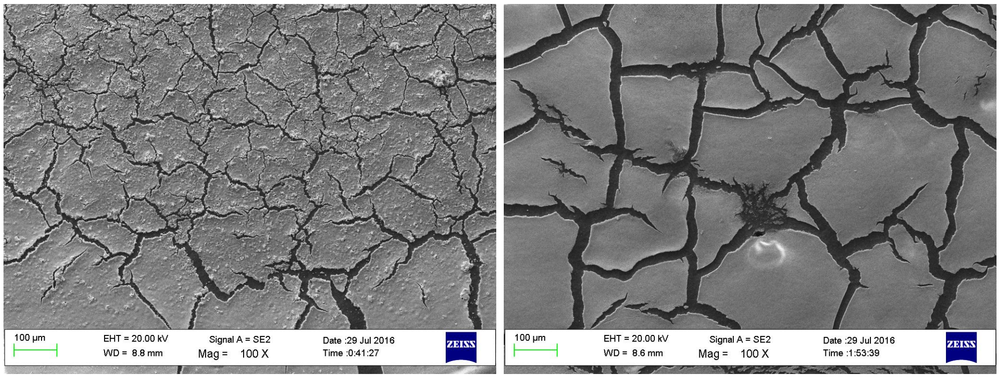

(a) Without settling at 100X **(b)** After setting separation at 100X

Figure 5.1: SEM images of drop casts onto carbon conductive tabs without separation 5.1a and with separation after settling for one hour 5.1b.

Putting forward a slightly more quantitative comparison: measuring a settling time of one hour and separating a suspension in ethanol for comparison of effects on spin coating. Both spin coatings were performed with the same acceleration and ran for twenty seconds at 2,000rpm. As can be seen in Figure 5.2, both high magnification (25,000X) images, Figures 5.2a and 5.2c, show a fairly similar distribution of nanoparticles; however, a clear distinction, and advantage, of the separation after settling for and hour is apparent in Figures 5.2b and 5.2d. At lower magnification (2,500X), one can clearly see large particles, over one micron, which would disrupt the ability to make a submicron film. Thus, it was decided to try filtration, a standard practice in spin coating film colloid preparation.

Paying note to quality issues observed in Figure 5.2, the discontinuity between nanoparticles has been well investigated, and causes are attributed to spin speeds that are too high [47]. Filtration with a 0.45-micron syringe filter was performed on a solution pulled from a 30-minute separation in ethanol. The solution appeared clear after filtration. Two step spin coating with thirty seconds at 500 rpm followed by thirty seconds at 2,000 rpm was used to deposit a film onto an Indium Tin Oxide (ITO) coated glass substrate. There were no large differences in film quality when deposited immediately after filtration versus four days later. Thus,

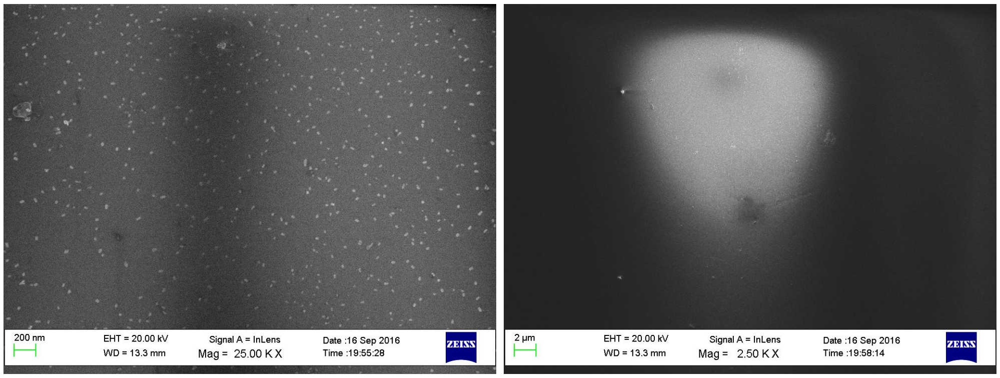

(a) After settling separation at 25,000X **(b)** After settling separation at 2,500X

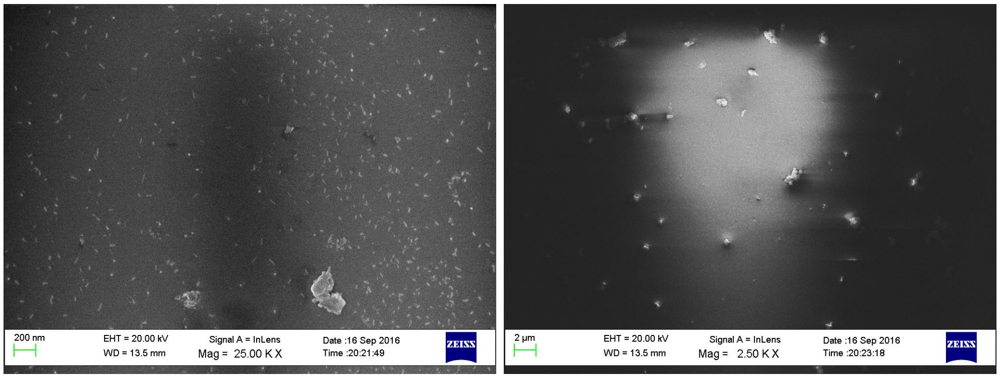

(c) Without settling at 25,000X **(d)** Without settling at 2,500X

Figure 5.2: SEM images of spin coats onto glass after settling separation 5.2a and 5.2b and without separation 5.2c and 5.2d.

agitation seems sufficient for suspension preparation, once large particles are removed, as agglomeration in ethanol or water does not appear to happen at a fast rate.

Heating the solution to try and create a higher weight percent of nanoparticles was performed at 50°C for varying times in an oven over two days, but with the evaporation seeming too slow, the temperature was raised to 60°C. This caused crystals to form while cooling. Those crystals were large and flat, as can be seen in Figure 5.3d. A ten coat film was made following the same single coat procedures, but adding a one minute heating of the film at 100°C on a hot plate between each

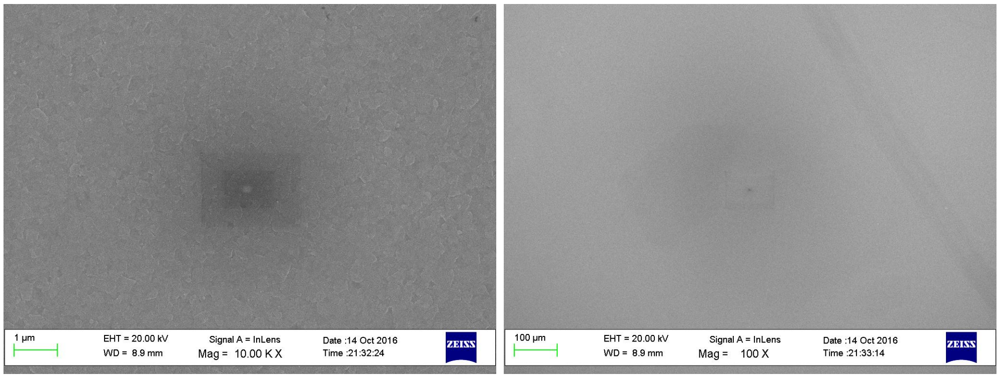

(a) After filtration at 10,000X **(b)** After filtration at 100X

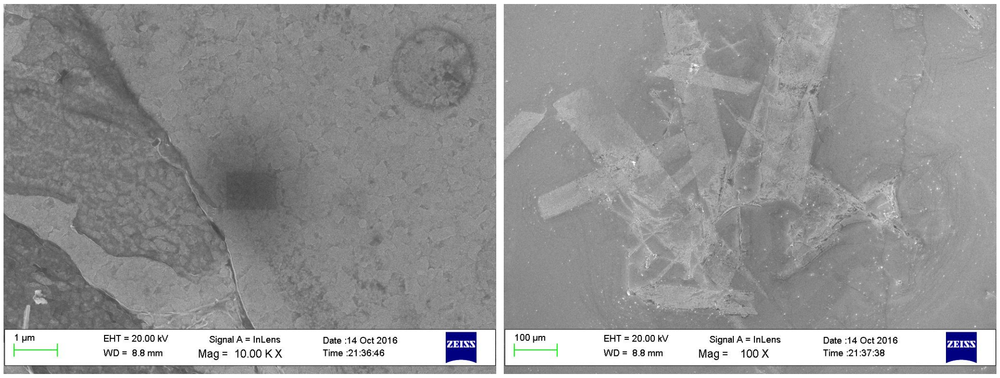

(c) After filtration and heating at 10,000X **(d)** After filtration and heating at 100X

Figure 5.3: SEM images of spin coats onto ITO coated glass after filtration 5.2a and 5.2b and heating 5.2c and 5.2d.

coat. This was done to ensure complete evaporation of the liquid and help secure each layer. A comparison of the film without the crystals and with them has been presented in Figure 5.3. Though one might believe them to also be quite thick; however, the films were still fairly transparent. Thus, this method was put on hold as it does not allow for thick enough films with the current product available from the outlined ball milling procedures in Chapter 4. Future plans for filtration of better fineness consistency product will commence once the ball milling machine returns to an operational status.

Seeing as even particle agglomerations could not lead to as significant ab-

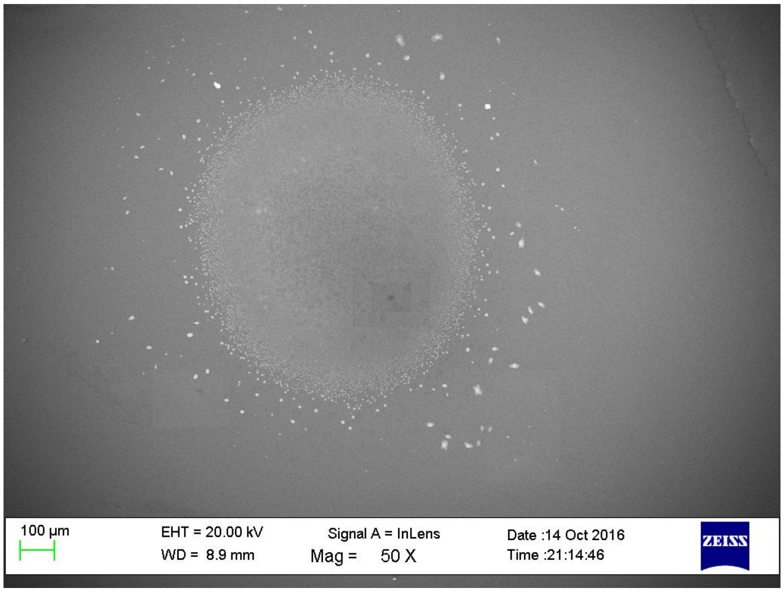

Figure 5.4: An agglomeration seen on a film post filtration at 50X.

sorption of light, as expected, at least 500-1,000 nanometer films would be more desirable. Wang et al. [47] mention contaminations such as dust causing nucleation sites for agglomerations. A similarly identified agglomeration is pointed out in Figure 5.4. However, such agglomerations are still too transparent. With a need for thicker films, but an inability to create high enough particle weights post filtration, drop casting seemed like a temporary alternative to try in order to test some prototype architectures.

5.2 Drop Casting

Drop casting was performed with various parameters in order to observe what would lead to the most uniform surface drop cast film. One example was the difference in weight ratios of product and liquid. Though the weight ratios seemed to make one of the larger impacts, other variables included the amount deposited, substrate temperature, and liquid for the suspension.

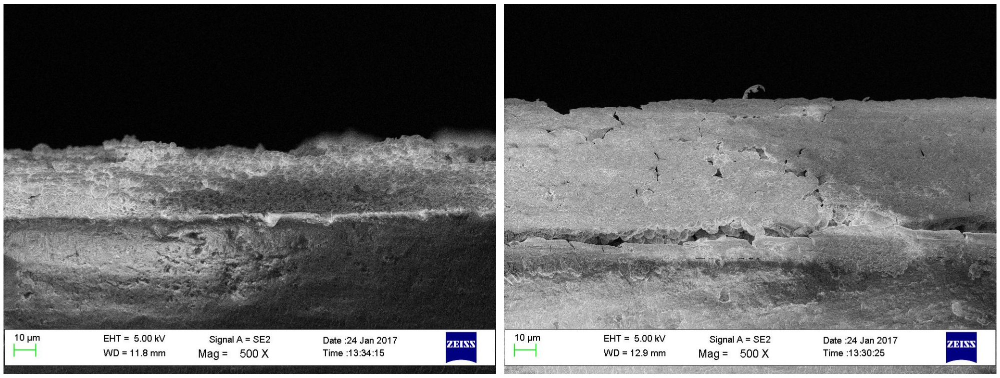

(a) Without heat at 500X

(b) 100°C heating at 500X

Figure 5.5: SEM images of drop casts onto glass without heat 5.5a and with heat 5.5b.

Higher weight ratios of product in liquid had a tendency to decrease film uniformity. Agglomerations would form in clusters on the film. While weight ratios much below 5% had a tendency to not fully coat the substrate. Instead, small island films would form on the substrate. Using water instead of ethanol seemed to help with having fewer agglomerations or islands. This could be due to a higher dipole moment as well as the density of water. This was one reason ethanol was chosen for separation of larger particles. The settling rate was significantly higher in ethanol when compared to water.

It can be seen in Figure 5.5 that heating the substrate does seem to cause grain growth during the drop cast. Though the thicknesses of the films are different, it is clear that heating helped with improving film density and crystallization. From this observation, doctor blading onto a heated substrate may be a nice option for good film quality.

In order to observe the difference in the amount deposited, multiple films were made at the same 5% weight ratio. The number of drops were counted for reference and later used to try and consistently make similar films. Ten drops are around half a milliliter. This was found to give good films for a 2 cm x 2 cm substrate. If just enough to coat the substrate was used, the meniscus shape was apparent in the film–thinner in the middle and thicker on the edges. Likewise, but to a lesser extent, a bulging amount would lead to a raised oval shape in the center. Thus, something in-between was found to be a good visual indicator for the amount to dispense. As stated this was around half a milliliter.

5.3 Film Characterization

Initially, visual inspection along with optical magnification was used to inspect uniformity of films. For the sake of quick measurement, simple transmission measurements were taken on film samples. Since the product is fairly matte, reflections are not necessarily a large issue. Also, the incident angle was kept near zero. Thus, characteristically, the absorption spectrum is going to be close to $100-$transmission. Transmission data has been reported as that is what was measured.

Using a xenon lamp sourced to a monochromator provided a selectable wavelength beam for transmission data. Transmission data was collected using an energy/power meter. Instruments were connected through a Source Measure Unit (SMU) and LabTracer 2.0 was used to control the data collection.

Background readings were collected through a blank glass slide and subtracted from the film readings. Measurements were taken in groups of three and averaged. The line was smoothed by a running three-point average. An example of a typical transmission profile for a film of Fe_2GeS_4 can be viewed in Graph 5.1. As can be seen in the comparison to the single crystal referenced spectrum [28], the onset rate is similar (the slopes are parallel). However, there are two, one that matches the onset of the previous work and a second slope. Previous theoretical absorption calculations show a similar profile [30]. This is likely due to the two band gap energies around 1.5 eV and a higher energy band gap of 2.6 eV as suggested by Ravichandran [31]. Here we see similar values around 1.6 eV and 2.0 eV from the onsets. The shift in values could be due to the size of the nanoparticles, crystallinity differences, as well as impurities.

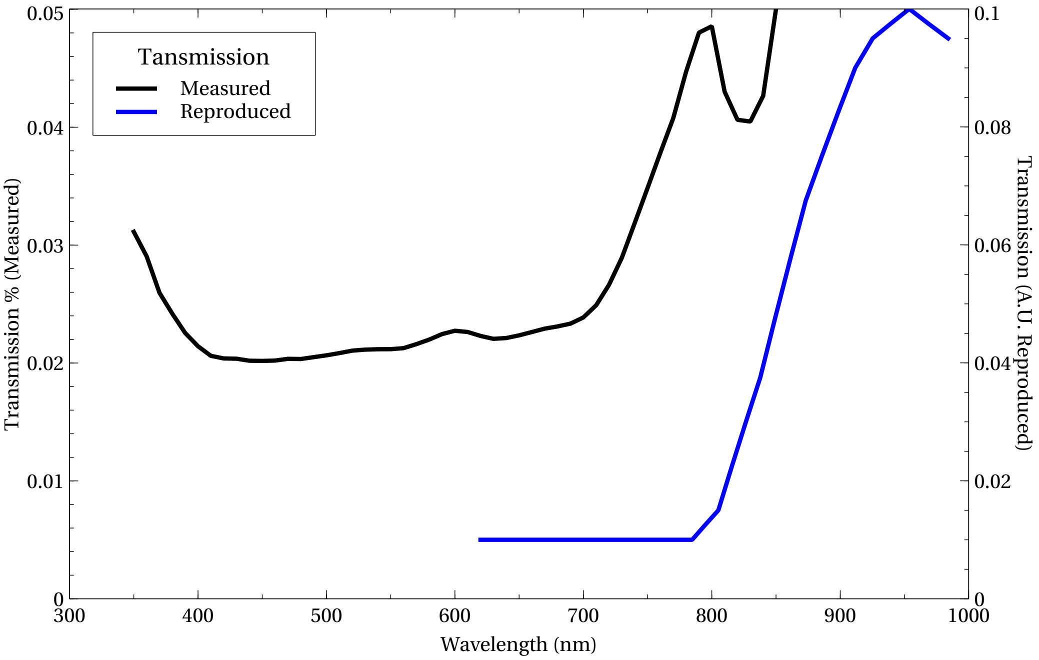

Graph 5.1: A typical film transmission spectrum compared with a single crystal transmission spectrum by Platt [28].

5.4 Prototype Characterization

Using the same SMU and software, current versus potential measurements were taken for various prototype architectures. For light measurements, the xenon lamp light was passed through a filter in order to simulate a natural sunlight spectrum (AM 1.5). Dark measurements were taken with lights off at night to minimize any light contamination. Shielding the sample with a dark cover in this atmosphere made little difference to the measurements. Since adding and removing the shield added the risk of bumping the connections to the electrodes, using the shield was determined as unnecessary in these conditions. A typical current versus potential prototype measurement is shown in Graph 5.2. With a quick calculation of the series and shunt resistances, it is clear that the series resistance is too high in all the devices. More on this will be discussed in Section 6.2. Where

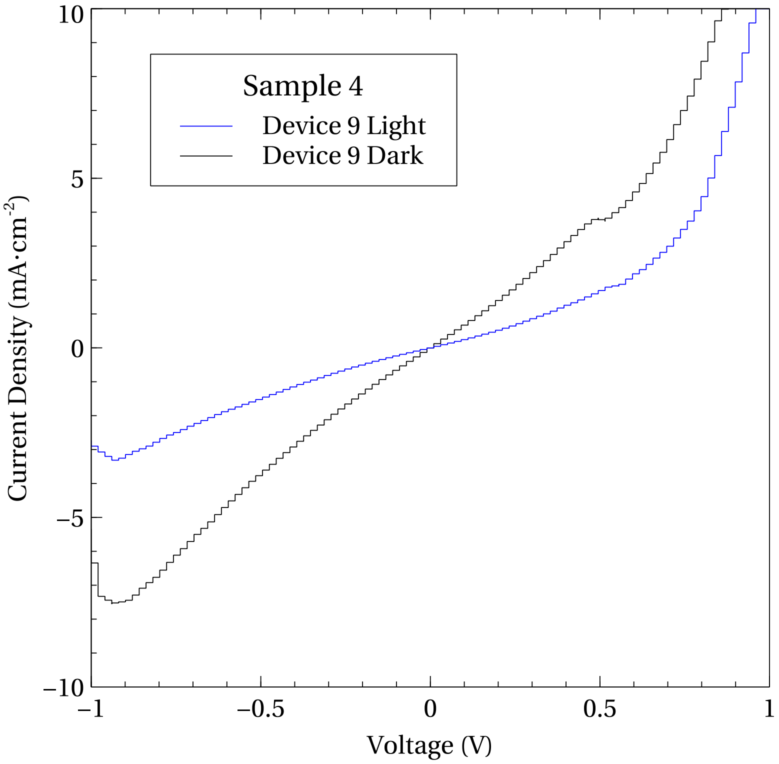

Graph 5.2: A typical prototype performance. $R_{SH} \sim 1-2\times10^4\Omega\cdot\text{cm}$ $R_S \sim 50\Omega\cdot\text{cm}^2$

possible, the shunt resistance (R_{SH}) has been calculated using the inverse of the slope at zero potential (V) divided by an estimated device thickness of 50-100 microns using the dark measurements. Using the second semi-linear region, after the start of the exponential rise in current, the series resistance (R_S) is calculated from the inverse of the slope; again, when possible, using the dark measurements.

Since the top electrodes, which had been evaporated onto the device, did not make good electrical contact, many of the first set of readings were done with an electrical probe resting on the back of the device. This does not allow for an accurate representation of the device area. So, contacts were painted over the evaporated contacts. This allowed for a proper connection to the side of the device

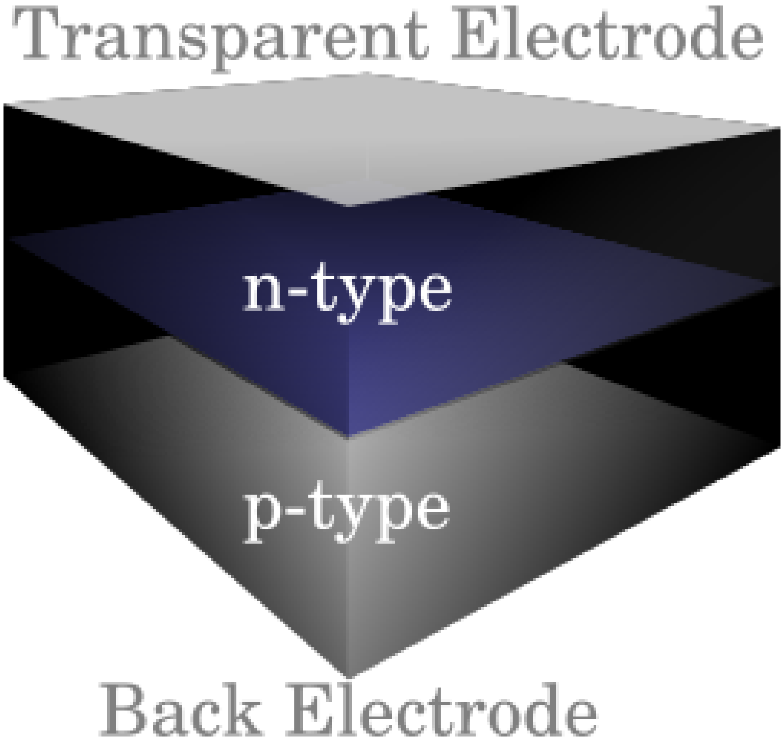

Figure 5.6: Prototype Architecture

with an electrical probe. As a means to observe phosphorus doping (which has yet to be done with this compound in any literature) and check it as a viable means of creating a solar cell with Fe_2GeS_4, various control experiments were set up. In describing these various setups, refer to Figure 5.6 for a visual on the various layers.

For all devices, the transparent electrode was ITO on a glass substrate. With only Fe_2GeS_4 as a p-type layer and silver as a back electrode, devices showed a resistor (linear) current versus potential curve as was expected. Adding a zinc oxide layer as an n-type window layer produce expected diode behavior as seen in Graph 5.3. The zinc oxide layers were prepared using a sol-gel process as described by Chou et al. [48]; however, spin coating was performed at 1000 rpm for 30 seconds followed by 60s at 2500 rpm to provide a thicker film. These architec-

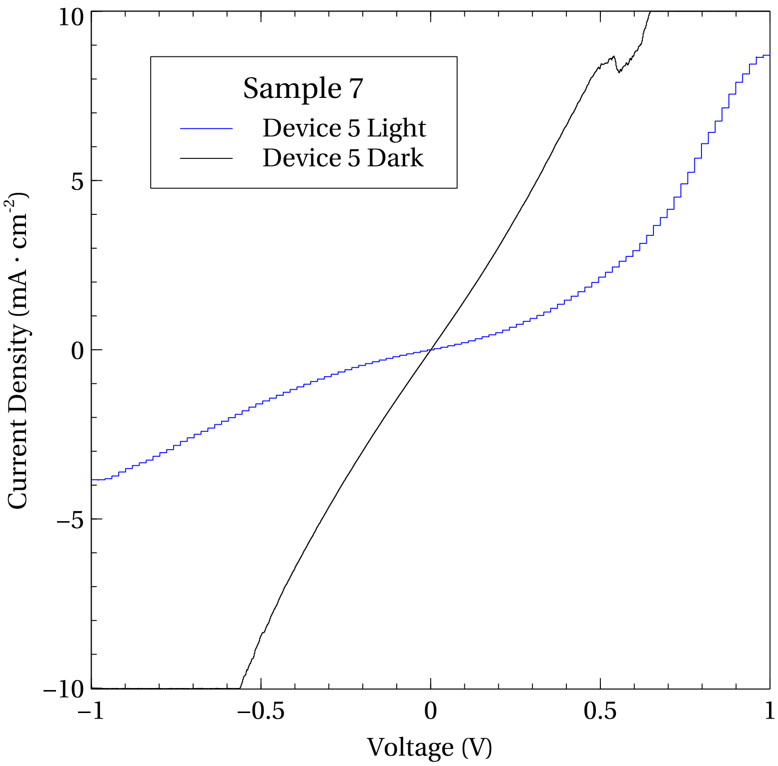

Graph 5.3: A typical prototype performance using a zinc oxide window layer. $R_{SH} \sim 5 - 10 \times 10^3 \Omega \cdot \mathrm{cm}$

tures showed little difference in performance compared with using a phosphorus doping for the n-type layer.

To test various doping levels using phosphoric acid, which has been successfully demonstrated on silicon wafers by Kim et al. [49], various acid concentrations were prepared. A moderated doping of 1 ppt ratio of phosphorus to Fe_2GeS_4 and a light doping of 1 ppm were both used. The diode response is sharper with a moderate doping as seen in Graph 5.4 in comparison to lighter doping, where the current onset is more gradual as seen in Graph 5.5.

To test the use of polyethylene glycol for stabilizing the colloid suspension and helping to bind the nanoparticles to the ITO layer, a solution was prepared

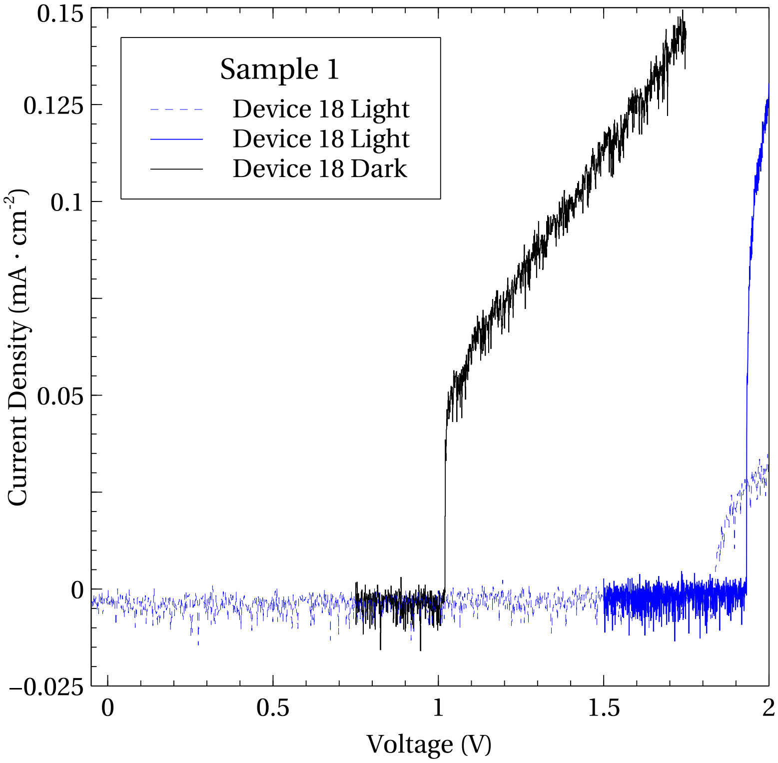

Graph 5.4: Moderate phosphorous doping prototype performance $R_S \sim 7 \times 10^3 \Omega \cdot \mathrm{cm}^2$

dissolved in ethanol. Rinses with deionized water, acetone, and isopropyl alcohol followed by hot plate heating were used to minimize contamination of the organic compound in the Fe_2GeS_4 nanoparticle film layer. Similar device performance as previously seen is shown in Graph 5.6.

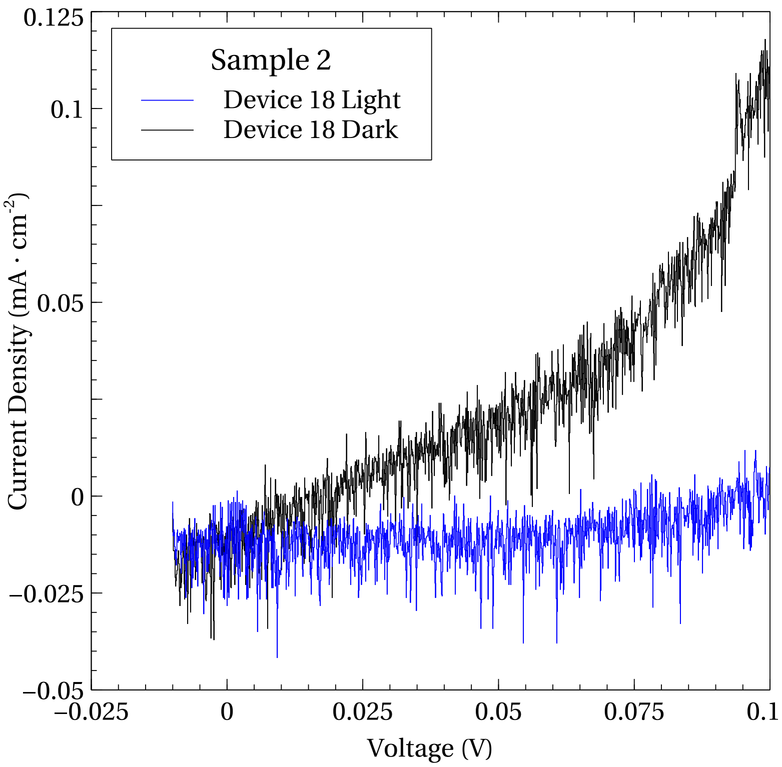

Graph 5.5: Light phosphorus doping prototype performance $R_{SH} \sim 1-2\times 10^5 \Omega \cdot \mathrm{cm}$ $R_S \sim 3\times 10^2 \Omega \cdot \mathrm{cm}^2$

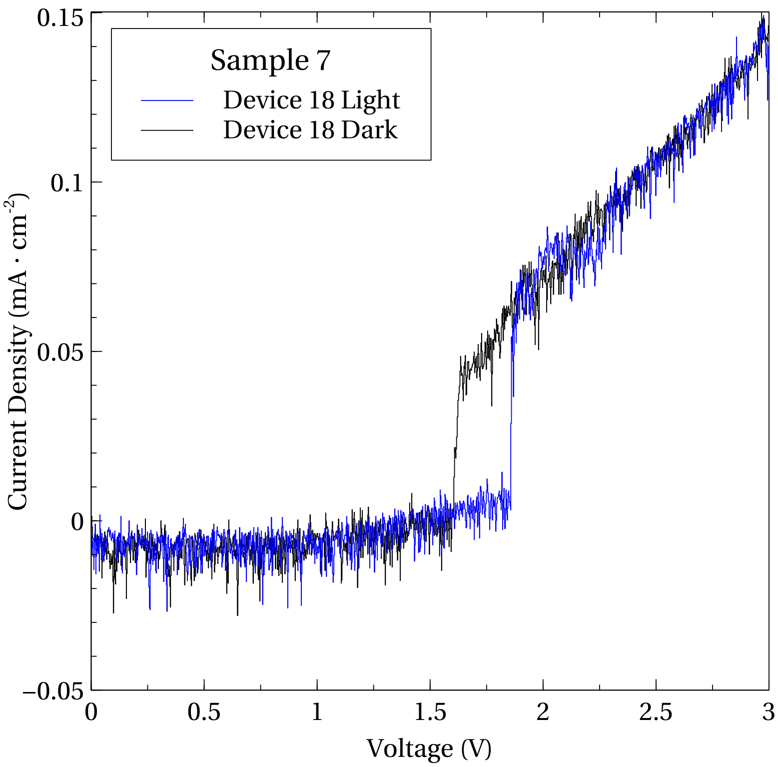

Graph 5.6: Light phosphorus doping with organic stabilizers used in spin coating prototype performance$R_{SH} \sim 1-3\times10^7\Omega\cdot\mathrm{cm}$ $R_s \sim 1\times10^4\Omega\cdot\mathrm{cm}^2$

Chapter 6

Conclusion

To the knowledge of the author, current existing literature does not contain any mechanochemical models which integrate reaction chemistry and mechanics without using abstract fitting parameters (dynamic fitting coefficients with no direct correlation to measurable factors within a process). Also, the successful implementation of mechanochemically synthesized Fe_2GeS_4 nanoparticles into a solar cell prototype has yet to be realized. Successes of preexisting works, which motivated these research endeavors, have been discussed in Section 2.4.

6.1 Expansion on Previous Works

In Chapter 3, a new model for mechanochemical synthesis is presented. It is found that this model is simple to use and easy to understand, which was the original goal. In Chapter 4, the feasibility and flexibility of Fe_2GeS_4 nanoparticle mechanochemical synthesis were confirmed. Various reaction boundaries were tested (milling parameters discussed in Chapter 4); however, more research is necessary to discern the full depth of options available while still achieving a successful synthesis. Chapter 5 expands on the successes achieved by Orefuwa et al. [50]. Their work presents a 6 mV open circuit potential and 0.3 $mA \cdot cm^{-2}$ short circuit current density. In Section 5.4, a photoresponse is observed with an open circuit potential many orders above that (between 1.5 and 2 V) and the diode response is sharper. However, the short circuit current is still small. A special note of significant accomplishments at this point go to the doping of a nanoparticle layer for the n-type layer. Not only is this a first time for this compound, but a method which may prove useful for other future solar cell designs.

6.2 Possible Limitations

In order to improve the model for use from its current generality, application to more specific experiments would make for a good opportunity to check the optimizing potential of such a model. Also, as it is designed for empirical fitting, it may take significant effort to produce a working, first principles example using the model. As for the experimental work, the synthesis could be matched with more chemical composition characterizations. This would provide more data for the model, as well as confirm various issues reported in preexisting works. It is possible that the Fe_2GeS_4 nanoparticles are heavily oxygen contaminated. Such impurities can help explain the small short circuit current observed in the final prototype.

Other issues, which could be plaguing the cells performance, mostly center on the thin film layer and the boundaries between layers. As can be seen in the values reported with Graphs 5.2 to 5.6, all of the shunt resistances are above $10^3\Omega\cdot$ cm and none of the series resistances are below $10\Omega\cdot\text{cm}^2$. At shunt resistance values below $10^3\Omega\cdot$cm, significant power loss becomes observable as the photon generated current is lost to the causes of the low resistance. Likely causes are material discontinuities. This can even be seen to drag down the open circuit potential as seen in graphs 5.2, 5.3 and 5.5 in comparison to Graphs 5.4 and 5.6 where the shunt resistance is higher. However, the real issue seems to be the high series resistance, as seen in all Graphs 5.2 to 5.6. A frequent issue causing this high value is often poor contact with the electrodes. This leads to a poor extraction of the light generated carriers from the inner layers, which ultimately has reduced the short circuit current to almost nothing in these devices. Another issue could be the extremely thick devices, which also lowers the probability of carrier collection by the electrodes. In Section 4.3 of their site info, Honsberg and Bowden [51] have some nice explanations of these issues along with interactive graphs to better grasp the effects of series and shunt resistance along with their impact on solar cell efficiency.

Many of the reasons for these resistance issues comes not only from the materials chosen, and how well they integrate with one another, but also the process of building a prototype. Without any high-temperature sintering, the films suffer from discontinuities caused by partially amorphous nanoparticles and poor connections between the particles. Discontinuities also exist from a lack of any surface passivation, which could also alleviate some of the oxygen contamination [32]. Finally, the film thickness and doping levels are far from optimized. It has been theoretically found, by Ravichandran [31], that for an optimal drift-cell configuration, something around a 750-nanometer thickness would be optimal. As the prototypes were more than 10 fold this thickness, collection probability for carriers was greatly decreased. Finally, the back electrode connection needs improvement as was demonstrated in Section 5.4.

6.3 Future Implications

With a working demonstration for a new theoretical mechanochemical synthesis model completed, options open up for expansion both within mechanochemistry and other fields. The final energy dependent terms could be tailored to an experiment by replacing the time with whatever dependence is necessary to accurately model size reduction. The amount of particle breaking could also be similarly tailored. To name a few options, current models pick up some fracture level (but remaining the same size), or changing size (decreasing if breaking and increasing if coalescing) by a matrix path [52], or neural network paths [53], or some Monte Carlo generated random option picks from a weighted list. Since all of these and many other models are already in place in the market, and this model has been generalized, it has potential application in various fields which study many types of syntheses. Not only do mechanochemical applications benefit from being able to use this model, but it is possible to apply theories for granular interactions and extend them to fluids based on concepts concerning viscosity. In short, energy input (in this case mechanical) can be paired with chemical dynamics using logic functions to model a system more completely.

As for the possibilities open to further work with Fe_2GeS_4 as a solar cell absorber, enough promise has been shown to rationalize investing more into investigating the use of this compound. Not only has surface passivation been shown to be effective [32], as well as hydrogen sulfide gas environment heat treatments to remove oxygen and improve nanoparticle crystallization [33], but work presented in Section 5.4 shows the possibility of doping the nanoparticles. The inability to do so successfully had previously prevented successful drift-cell configurations [31]. Improvements to the mechanochemical synthesis can likely benefit from milling optimization. That includes using a solid diluent [14] to reduce reaction speed, as would be predicted by the model in Chapter 3, the reaction can be slowed by hindering collisions between reactants. This is one way to improve final particle size and uniformity. With investments into good nanoparticle production, better results should be realizable for thin film deposition. Many methods exist for depositing nanoparticle. Proper optimization starts with stabilizing a colloid suspension. Though various means were explored for doing so, ultimately it was decided to move forward with a prototype without optimizing a film in order to validate further research into using Fe_2GeS_4 nanoparticles for a solar cell absorber layer. With the positive results, it would now be appropriate to extend the work done in Chapter 5. As suggested in Section 5.2, doctor blading may be a nice option for this compound. Such an option keeps with the theme of green manufacturing (low waste) and easy scalability. Thus, the question of whether Fe_2GeS_4 will be the answer to cheap electricity produced by solar energy harvesting remains unanswered, but more is known about the possibilities and the compound shows promise for future work.

Bibliography

[1] Ezekiel. *Book of the Prophet Ezekiel in The Holy Bible: King James Version*. Trident Reference Publishing, 2007. ISBN 1600810861. → pages 1

[2] K. Kuehn. *A Student's Guide Through the Great Physics Texts: Volume III: Electricity, Magnetism and Light*. Undergraduate Lecture Notes in Physics. Springer International Publishing, 2015. ISBN 9783319218168. → pages 2

[3] M.H. Shamos. *Great Experiments in Physics: Firsthand Accounts from Galileo to Einstein*. Dover classics of science and mathematics. Dover Publications, 1959. ISBN 9780486253466. → pages 2

[4] D. Kim, K. Seo, W. Choi, M. Kim, U. Kang, S. Ju, and W. Choi. Detection of evanescent waves using disordered nanowires. *Optics Communications*, 297:1–6, 2013. ISSN 0030-4018. doi:10.1016/j.optcom.2013.01.050. URL http://www.sciencedirect.com/science/article/pii/S0030401813001338. → pages 2

[5] D. A. Papathanassoglou and B. Vohnsen. Direct visualization of evanescent optical waves. *American Journal of Physics"*, 71(7):670–677, 2003. doi:10.1119/1.1564811. URL http://scitation.aip.org/content/aapt/journal/ajp/71/7/10.1119/1.1564811. → pages 2

[6] A.E. Becquerel. Recherches sur les effets de la radiation chimique de la lumiere solaire au moyen des courants electriques. *Comptes Rendus de L'Academie des Sciences*, 9:145–149, 1839. → pages 4

[7] W.G. Adams and R.E. Day. The action of light on selenium. *Proceedings of the Royal Society, London*, A25:113, 1877. → pages 4

[8] R.S. Ohl. Light-sensitive electric device, June 1946. URL http://www.google.ca/patents/US2402662. US Patent 2,402,662. → pages 4

[9] D. M. Chapin, C. S. Fuller, and G. L. Pearson. A new silicon pn junction photocell for converting solar radiation into electrical power. *Journal of Applied Physics*, 25(5):676–677, 1954. doi:10.1063/1.1721711. URL http://scitation.aip.org/content/aip/journal/jap/25/5/10.1063/1.1721711. → pages 4

[10] United States Department of Energy. Photovoltaics research and development. http://energy.gov/eere/sunshot/photovoltaics-research-and-development, 2016. URL http://energy.gov/. Retrieved October 15, 2016. → pages 4

[11] National Renewable Energy Laboratory. Materials and devices. http://www.nrel.gov/pv/materials-devices.html, 2016. URL http://www.nrel.gov/. Retrieved October 15, 2016. → pages 4

[12] National Renewable Energy Laboratory. Best research-cell efficiencies. http://www.nrel.gov/pv/assets/images/efficiency_chart.jpg, 2016. URL http://www.nrel.gov/. Retrieved October 15, 2016. → pages x, 5

[13] K. Mertens. *Photovoltaics : Fundamentals, Technology and Practice (1)*. Wiley, 2013. ISBN 9781118703366. → pages 9

[14] T. Tsuzuki and P. G. McCormick. Mechanochemical synthesis of nanoparticles. *Journal of Materials Science*, 39(16):5143–5146, 2004. ISSN 1573-4803. doi:10.1023/B:JMSC.0000039199.56155.f9. → pages 9, 12, 92

[15] P.P. Chin, J. Ding, J.B. Yi, and B.H. Liu. Synthesis of fes2 and fes nanoparticles by high-energy mechanical milling and mechanochemical processing. *Journal of Alloys and Compounds*, 390(1-2):255 – 260, 2005. ISSN 0925-8388. doi:10.1016/j.jallcom.2004.07.053. URL http://www.sciencedirect.com/science/article/pii/S0925838804010783. → pages 12

[16] R. F. Egerton. *Physical Principles of Electron Microscopy: An Introduction to TEM, SEM, and AEM*. Springer International Publishing, Cham, 2016. ISBN 978-3-319-39877-8. doi:10.1007/978-3-319-39877-8_4. → pages 14

[17] H. Borchert. *Solar Cells Based on Colloidal Nanocrystals*. Springer International Publishing, Cham, 2014. ISBN 978-3-319-04388-3. doi:10.1007/978-3-319-04388-3_5. → pages 14

[18] R. Jenkins and R. L. Snyder. *Introduction to X-ray Powder Diffractometry*. John Wiley & Sons, Inc., 1996. ISBN 9781118520994. doi:10.1002/9781118520994. → pages 16, 18

[19] World Health Organization. The world health report 2002–reducing risks, promoting healthy life. Technical report, World Health Organization, 2002. URL http://www.who.int/en/. → pages x, 26

[20] World Health Organization. Breathelife. http://breathelife2030.org/, 2016. URL http://breathelife2030.org/. Retrieved December 12, 2016. → pages 25, 26

[21] United Nations. Transforming our world: the 2030 agenda for sustainable development. Technical report, United Nations, 2015. URL http://www.un.org/. → pages 27

[22] M. Perez and R. Perez. Update 2015a fundamental look at supply side energy reserves for the planet. *The IEA SHC Solar Update*, 62, 2015. URL http://asrc.albany.edu/people/faculty/perez/2015/IEA.pdf. → pages xi, 28

[23] SunShot. Sunshot 2020 goals. http://energy.gov/eere/sunshot/sunshot-initiative-goals, 2016. URL http://energy.gov/. Retrieved December 12, 2016. → pages 28

[24] H. Vincent, E. F. Bertaut, W. H. Baur, and R. D. Shannon. Polyhedral deformations in olivine-type compounds and the crystal structure of fe_2sis_4 and fe_2ges_4. *Acta Crystallographica Section B*, 32(6):1749–1755, June 1976. doi:10.1107/S056774087600633X. → pages 30

[25] J.-C. Jumas, E. Philippot, and M. Maurin. Etude structurale d'un thiospinelle d'étain fe_2sns_4. *Acta Crystallographica Section B*, 33(12): 3850–3854, December 1977. doi:10.1107/S0567740877012205. → pages 30

[26] A. Junod, K.-Q. Wang, G. Triscone, and G. Lamarche. Specific heat, magnetic properties and critical behaviour of mn2sis4 and fe2ges4. *Journal of Magnetism and Magnetic Materials*, 146(1):21 – 29, 1995. ISSN

0304-8853. doi:10.1016/0304-8853(94)01665-8. URL http://www.sciencedirect.com/science/article/pii/0304885394016658. → pages 30

[27] J. A. Spies. *Inorganic Thin-Film Solar Cells*. MASc thesis, Oregon State University, 2007. URL http://hdl.handle.net/1957/7125. → pages 30

[28] H. A. S. Platt. *Copper and Iron Chalcogenides for Efficient Solar Absorption*. PhD dissertation, Oregon State University, 2010. URL http://hdl.handle.net/1957/15009. → pages xiii, 30, 81, 82

[29] L. Yu, S. Lany, R. Kykyneshi, V. Jieratum, R. Ravichandran, B. Pelatt, E. Altschul, H. A. S. Platt, J. F. Wager, D. A. Keszler, and A. Zunger. Iron chalcogenide photovoltaic absorbers. *Advanced Energy Materials*, 1(5): 748–753, August 2011. ISSN 1614-6840. doi:10.1002/aenm.201100351. → pages 30, 36, 39

[30] B. D. Pelatt. *Atomic Solid State Energy Scale Applied to Novel Thin-Film Solar Absorbers*. PhD dissertation, Oregon State University, 2013. URL http://hdl.handle.net/1957/40673. → pages 30, 31, 81

[31] R. Ravichandran. *Development of High Efficiency Solar Absorbers*. PhD dissertation, Oregon State University, 2014. URL http://hdl.handle.net/1957/48898. → pages 31, 81, 91, 92

[32] S. J. Fredrick and A. L. Prieto. Solution synthesis and reactivity of colloidal fe2ges4: A potential candidate for earth abundant, nanostructured photovoltaics. *Journal of the American Chemical Society*, 135(49): 18256–18259, 2013. doi:10.1021/ja408333y. → pages 31, 91, 92

[33] B. Park, S. Yu, Y. Hwang, S. Cho, J. Lee, C. Park, D. Lee, and S. Y. Lee. Highly crystalline fe2ges4 nanocrystals: green synthesis and their structural and optical characterization. *J. Mater. Chem. A*, 3:2265–2270, 2015. doi:10.1039/C4TA05850J. URL http://dx.doi.org/10.1039/C4TA05850J. → pages 31, 39, 49, 50, 60, 61, 92

[34] D. Lim, P. Ramasamy, and J. Lee. Solution synthesis of single-crystalline fe2ges4 nanosheets. *Materials Letters*, 183:65 – 68, 2016. ISSN 0167-577X. doi:10.1016/j.matlet.2016.07.072. URL http://www.sciencedirect.com/science/article/pii/S0167577X16311764. → pages 31

[35] C. Cuadrado-Laborde, L.C. Damonte, and L. Mendoza-Zlis. Theoretical treatment of a self-sustained, ball milling induced, mechanochemical reaction in the Fe_2O_3–Al system. *Materials Science and Engineering: A*, 355(12):106–113, August 2003. ISSN 0921-5093. doi:10.1016/S0921-5093(03)00075-3. → pages 34

[36] S. Fadda, A. Cincotti, A. Concas, M. Pisu, and G. Cao. Modelling breakage and reagglomeration during fine dry grinding in ball milling devices. *Powder Technology*, 194(3):207–216, September 2009. ISSN 0032-5910. doi:10.1016/j.powtec.2009.04.009. → pages 34

[37] F.L. Cumbrera and F. Snchez-Bajo. Transition phenomena in condensed matter the use of the JMAYK kinetic equation for the analysis of solid-state reactions: critical considerations and recent interpretations. *Thermochimica Acta*, 266:315–330, November 1995. ISSN 0040-6031. doi:10.1016/0040-6031(95)02554-5. → pages 34

[38] H. Tanaka. Calorimetry and thermal analysis thermal analysis and kinetics of solid state reactions. *Thermochimica Acta*, 267:29–44, December 1995. ISSN 0040-6031. doi:10.1016/0040-6031(95)02464-6. → pages

[39] A. Khawam and D. R. Flanagan. Solid-state kinetic models: basics and mathematical fundamentals. *The Journal of Physical Chemistry B*, 110(35): 17315–17328, 2006. doi:10.1021/jp062746a. PMID: 16942065. → pages 34

[40] G. R. Williams and D. O'Hare. A kinetic study of the intercalation of lithium salts into $Al(OH)_3$. *The Journal of Physical Chemistry B*, 110(22): 10619–10629, 2006. doi:10.1021/jp057130k. PMID: 16771307. → pages 34, 52

[41] T. Hao. Analogous viscosity equations of granular powders based on eyring's rate process theory and free volume concept. *RSC Adv.*, 5: 95318–95333, October 2015. doi:10.1039/C5RA16706J. → pages 35, 49

[42] J. E. House. *Principles of Chemical Kinetics*. Elsevier/Academic Press, 2nd edition, 2007. → pages 38, 40

[43] L. Takacs. Self-sustaining reactions induced by ball milling. *Progress in Materials Science*, 47(4):355–414, 2002. ISSN 0079-6425. doi:10.1016/S0079-6425(01)00002-0. → pages 52

[44] P. Balz and SpringerLink ebooks - Chemistry and Materials Science. *Mechanochemistry in Nanoscience and Minerals Engineering*. Springer, New York, 1. aufl. edition, 2008. ISBN 3540748547;9783540748540;9783642094262;3642094260;. → pages 57

[45] Y. Zhao and J. S. Marshall. Spin coating of a colloidal suspension. *Physics of Fluids*, 20(4):043302, 2008. ISSN 10706631. URL http://search.ebscohost.com.ezproxy.library.ubc.ca/login.aspx?direct=true&db=a9h&AN=31881721&site=ehost-live&scope=site. → pages 75

[46] M.D. Tyona. A theoritical study on spin coating technique. *Advances in materials Research*, 2:195–208, 2013. doi:10.12989/amr.2013.2.4.195. URL http://koreascience.or.kr/article/ArticleFullRecord.jsp?cn=TPTPLG_2013_v2n4_195. → pages 75

[47] Q. Wang, L. Ye, L. Wang, P. Li, Y. Cao, and Y. Li. Rapid nanopatterning technique based on monolayer silica nanosphere close-packing by spin coating. *Science China Technological Sciences*, 59(10):1573–1580, 2016. ISSN 1869-1900. doi:10.1007/s11431-016-0316-2. → pages 75, 76, 79

[48] C. Chou, W. L. Kwan, Z. Hong, L. Chen, and Y. Yang. A metal-oxide interconnection layer for polymer tandem solar cells with an inverted architecture. *Advanced Materials*, 23(10):1282–1286, 2011. ISSN 1521-4095. doi:10.1002/adma.201001033. → pages 84

[49] D. S. Kim, M. M. Hilali, A. Rohatgi, K. Nakano, A. Hariharan, and K. Matthei. Development of a phosphorus spray diffusion system for low-cost silicon solar cells. *Journal of The Electrochemical Society*, 153(7): A1391–A1396, 2006. doi:10.1149/1.2202088. URL http://jes.ecsdl.org/content/153/7/A1391.abstract. → pages 85

[50] S. A. Orefuwa, C. Lai, K. Dobson, C. Ni, and D. Radu. Novel solution process for fabricating ultra-thin-film absorber layers in fe2sis4 and fe2ges4 photovoltaics. *MRS Proceedings*, 1670, 2014. → pages 89

[51] C. Honsberg and S. Bowden. The photovoltaic education network, 2017. URL http://pveducation.org/. Retrieved April 4, 2017. → pages 91

[52] V. Monov, B. Sokolov, and S. Stoenchev. Grinding in ball mills: Modeling and process control. *Cybernetics and Information Technologies*, 12(2):

51–68, March 2013. ISSN 1311-9702. doi:10.2478/cait-2012-0012. → pages 91

[53] V. Singh, P. K. Banerjee, S. K. Tripathy, V. K. Saxena, and R. Venugopal. Artificial neural network modeling of ball mill grinding process. *Journal of Powder Metallurgy & Mining*, 2(2):1–4, 2013. ISSN 2168-9806. doi:10.4172/2168-9806.1000106. → pages 91

Appendix A

Supporting Materials

A.1 Code

This code generates a column printing of all the desired parameters for generating a graph from a data file using fourth order Runge-Kutta for numeric approximation. Parameters for changing the output match the parameters listed in Chapter 3. The differential equations in the ”Define the ODE” section match the final set of differential equations from Section 3.4.

```
#include <stdio.h>
#include <math.h>
#include <stdlib.h>

/*************************************/
/* Parameters you may want to change */
/*************************************/

#define N 11 /* Number of First Order Equations */

#define DELTA_T 0.001 /* Stepsize in t */

#define INITIAL_Y3 0 /* Initial Iron Sulfide */
#define INITIAL_Y4 0 /* Initial Germanium Sulfide */
#define INITIAL_Y5 0 /* Initial Compound */

#define INITIAL_Y6 1*1.0/pow(10.0,6) /* Initial Paticle Radius */
#define INITIAL_Y7 1*1.0/pow(10.0,6) /* Initial Paticle Radius */
```

```
#define INITIAL_Y8 1*1.0/pow(10.0,6) /* Initial Paticle Radius */
#define INITIAL_Y9 1*1.0/pow(10.0,6) /* Initial Paticle Radius */
#define INITIAL_Y10 1*1.0/pow(10.0,6) /* Initial Paticle Radius */

#define MFe 55.8450 /* Fe g/mol */
#define MS 32.0650 /* S g/mol */
#define MGe 72.6400 /* Ge g/mol */
#define MFeS 87.9100 /* FeS g/mol */
#define MGeS2 136.7700 /* GeS2 g/mol */
#define MFe2GeS4 312.5900 /* Fe2GeS4 g/mol */

#define PFe2GeS4 5.0 /* Produced Fe2GeS4 g */

#define KFeS 10.0 /* FeS Rate Lmol-1s-1 */
#define KGeS2 10.0 /* GeS2 Rate L2mol-2s-1 */
#define KFe2GeS4 10.0 /* Fe2GeS4 rate L2mol-2s-1 */

#define Vol 0.050 /* Jar Volume L */

#define RFecrit 200*1.0/pow(10.0,9) /* Critical Radius */
#define RGecrit 200*1.0/pow(10.0,9) /* Critical Radius */
#define RScrit 200*1.0/pow(10.0,9) /* Critical Radius */
#define RFeScrit 200*1.0/pow(10.0,9) /* Critical Radius */
#define RGeS2crit 200*1.0/pow(10.0,9) /* Critical Radius */

#define WFe 1.0*pow(10.0,12) /* Arctangent Slope */
#define WGe 1.0*pow(10.0,12) /* Arctangent Slope */
#define WS 1.0*pow(10.0,12) /* Arctangent Slope */
#define WFeS 1.0*pow(10.0,10) /* Arctangent Slope */
#define WGeS2 1.0*pow(10.0,10) /* Arctangent Slope */

#define BFe -log(0.70) /* Break Fraction */
#define BGe -log(0.40) /* Break Fraction */
#define BS -log(0.85) /* Break Fraction */
#define BFeS -log(0.30) /* Break Fraction */
#define BGeS2 -log(0.35) /* Break Fraction */

#define EFe log(.2)/(6.0*3600*log(0.70)) /* E Breaking Coefficient */
#define EGe log(.2)/(9.0*3600*log(0.40)) /* E Breaking Coefficient */
#define ES log(.2)/(3.0*3600*log(0.85)) /* E Breaking Coefficient */
#define EFeS log(.2)/(12.0*3600*log(0.30)) /* E Breaking Coefficient */
#define EGeS2 log(.2)/(11.0*3600*log(0.35)) /* E Breaking Coefficient */

#define nFe 10 /* Sine Function Power */
#define nGe 10 /* Sine Function Power */
#define nS 10 /* Sine Function Power */
```

```
#define nFeS 10 /* Sine Function Power */
#define nGeS2 10 /* Sine Function Power */

/***************************************/
/* Double factorial fraction n!!/(n-1)!! */
/***************************************/

double norm(double z){

        double i, num, den;

        num=1.0;

        for(i=z;i>=1;i-=2){
                num *=i;
        }

        den=1.0;

        for(i=z-1;i>=1;i-=2){
                den *=i;
        }

        return num/den;
}

/****************/
/* Define the ODE */
/****************/

double f(double x, double y[], int i) {

        double RFedep, RGedep, RSdep, RFeSdep, RGeS2dep, RFeScoef, RGeS2coef,
             RFe2GeS4coef;

        RFedep = 0.5+atan(WFe*(RFecrit-y[6]))/M_PI;
        RGedep = 0.5+atan(WGe*(RGecrit-y[7]))/M_PI;
        RSdep = 0.5+atan(WS*(RScrit-y[8]))/M_PI;
        RFeSdep = 0.5+atan(WFeS*(RFeScrit-y[9]))/M_PI;
        RGeS2dep = 0.5+atan(WGeS2*(RGeS2crit-y[10]))/M_PI;

        RFeScoef = RFedep*RSdep;
        RGeS2coef = RGedep*RSdep;
        RFe2GeS4coef = RFeSdep*RGeS2dep;

        if (i==0) return
```

```
-RFeScoef*KFeS*y[0]*y[2]; /* dFe/dt */

if (i==1) return

-RGeS2coef*KGeS2*y[1]*y[2]*y[2]; /* dGe/dt */

if (i==2) return

-RFeScoef*KFeS*y[0]*y[2]-2*RGeS2coef*KGeS2*y[1]*y[2]*y[2]; /* dS/dt */

if (i==3) return

RFeScoef*KFeS*y[0]*y[2]-2*RFe2GeS4coef*KFe2GeS4*y[3]*y[3]*y[4]; /* dFeS/dt */

if (i==4) return

RGeS2coef*KGeS2*y[1]*y[2]*y[2]-RFe2GeS4coef*KFe2GeS4*y[3]*y[3]*y[4]; /* dGeS2/dt
        */

if (i==5) return

RFe2GeS4coef*KFe2GeS4*y[3]*y[3]*y[4]; /* dFe2GeS4/dt */

if (i==6) return

-y[6]*(norm(nFe))*EFe*(BFe)*pow(sin(M_PI*x*EFe),nFe); /* dRFe/dt */

if (i==7) return

-y[7]*(norm(nGe))*EGe*(BGe)*pow(sin(M_PI*x*EGe),nGe); /* dRGe/dt */

if (i==8) return

-y[8]*(norm(nS))*ES*(BS)*pow(sin(M_PI*x*ES),nS); /* dRS/dt */

if (i==9) return

-y[9]*(norm(nFeS))*EFeS*(BFeS)*pow(sin(M_PI*x*EFeS),nFeS); /* dRFeS/dt */

if (i==10) return

-y[10]*(norm(nGeS2))*EGeS2*(BGeS2)*pow(sin(M_PI*x*EGeS2),nGeS2); /* dRGeS3/dt */

else return 0;
```

```
}

/****************/
/* Main Function */
/****************/

int main(void){

        double t, y[N],Produced;

        int count;

        void runge4(double x, double y[], double step); /* Runge-Kutta function */

        Produced=PFe2GeS4/MFe2GeS4;

        y[0]=2*Produced/Vol; /* initial Y[0] */
        y[1]=Produced/Vol; /* initial Y[1] */
        y[2]=4*Produced/Vol; /* initial Y[2] */

        y[3]=INITIAL_Y3; /* initial Y[3] */
        y[4]=INITIAL_Y4; /* initial Y[4] */
        y[5]=INITIAL_Y5; /* initial Y[5] */
        y[6]=INITIAL_Y6; /* initial Y[6] */
        y[7]=INITIAL_Y6; /* initial Y[7] */
        y[8]=INITIAL_Y6; /* initial Y[8] */
        y[9]=INITIAL_Y6; /* initial Y[9] */
        y[10]=INITIAL_Y6; /* initial Y[10] */

        count=-1;

        printf("Time\tIron\tGermanium\tSulfur\tIron Sulfide\tGermanium Sulfide\tFe2GeS4\
             tS/Fe\tS/Ge\tRFe\tRGe\tRS\tRFeS\tRGeS2\tRFedep\tRGedep\tRSdep\tRFeSdep\
             tRGeS2dep\n");

        /* column labels */

        printf("%lf\t%lf\t%lf\t%lf\t%lf\t%lf\t%lf\t%lf\t%lf\t%lf\t%lf\t%lf\t%lf\t%lf\t%
             lf\t%lf\t%lf\t%lf\t%lf\n",0.0,y[0]*MFe*Vol/PFe2GeS4,
        y[1]*MGe*Vol/PFe2GeS4,y[2]*MS*Vol/PFe2GeS4,y[3]*MFeS*Vol/PFe2GeS4,
        y[4]*MGeS2*Vol/PFe2GeS4,y[5]*MFe2GeS4*Vol/PFe2GeS4,
        (y[2]+y[3]+2*y[4]+4*y[5])/(y[0]+y[3]+2*y[5]),(y[2]+y[3]+2*y[4]+4*y[5])/(y[1]+y
             [4]+y[5]),
        y[6]*pow(10.0,9),y[7]*pow(10.0,9),y[8]*pow(10.0,9),y[9]*pow(10.0,9),y[10]*pow
             (10.0,9),
```

```
0.5+atan(WFe*(RFecrit-y[6]))/M_PI,0.5+atan(WGe*(RGecrit-y[7]))/M_PI,0.5+atan(WS
      *(RScrit-y[8]))/M_PI,
0.5+atan(WFeS*(RFeScrit-y[9]))/M_PI,0.5+atan(WGeS2*(RGeS2crit-y[10]))/M_PI);

/*************/
/* Time Loop */
/*************/

for (t=0; t<54000; t+=DELTA_T) {

        if(y[0]<0){
                y[0]=0;
        }

        if(y[1]<0){
                y[1]=0;
        }

        if(y[2]<0){
                y[2]=0;
        }

        if(y[3]<0){
                y[3]=0;
        }

        if(y[4]<0){
                y[4]=0;
        }

        if(y[5]<0){
                y[5]=0;
        }

        if(y[6]<0){
                y[6]=0;
        }

        if(y[7]<0){
                y[7]=0;
        }

        if(y[8]<0){
                y[8]=0;
        }
```

```
                if(y[9]<0){
                        y[9]=0;
                }

                if(y[10]<0){
                        y[10]=0;
                }

                runge4(t, y, DELTA_T);

                count++;

                if (count==10000){

                        printf(”%lf\t%lf\t%lf\t%lf\t%lf\t%lf\t%lf\t%lf\t%lf\t%lf\t%lf\t%
                              lf\t%lf\t%lf\t%lf\t%lf\t%lf\t%lf\t%lf\n”,t/3600,y[0]*MFe*
                              Vol/PFe2GeS4,
                        y[1]*MGe*Vol/PFe2GeS4,y[2]*MS*Vol/PFe2GeS4,y[3]*MFeS*Vol/
                              PFe2GeS4,
                        y[4]*MGeS2*Vol/PFe2GeS4,y[5]*MFe2GeS4*Vol/PFe2GeS4,
                        (y[2]+y[3]+2*y[4]+4*y[5])/(y[0]+y[3]+2*y[5]),(y[2]+y[3]+2*y
                              [4]+4*y[5])/(y[1]+y[4]+y[5]),
                        y[6]*pow(10.0,9),y[7]*pow(10.0,9),y[8]*pow(10.0,9),y[9]*pow
                              (10.0,9),y[10]*pow(10.0,9),
                        0.5+atan(WFe*(RFecrit-y[6]))/M_PI,0.5+atan(WGe*(RGecrit-y[7]))/
                              M_PI,0.5+atan(WS*(RScrit-y[8]))/M_PI,
                        0.5+atan(WFeS*(RFeScrit-y[9]))/M_PI,0.5+atan(WGeS2*(RGeS2crit-y
                              [10]))/M_PI);

                        count=0;
                }
        }
        return 0;
}

/************/
/* RK4 Loop */
/************/

void runge4(double x, double y[], double step) {
        double h=step/2.0;                      /* the midpoint */
        double t1[N], t2[N], t3[N];             /* temporary storage arrays */
        double k1[N], k2[N], k3[N],k4[N];       /* for Runge-Kutta */
        int i;

        for (i=0;i<N;i++) t1[i]=y[i]+0.5*(k1[i]=step*f(x, y, i));
```

```
        for (i=0;i<N;i++) t2[i]=y[i]+0.5*(k2[i]=step*f(x+h, t1, i));
        for (i=0;i<N;i++) t3[i]=y[i]+    (k3[i]=step*f(x+h, t2, i));
        for (i=0;i<N;i++) k4[i]=                step*f(x+step, t3, i);

        for (i=0;i<N;i++) y[i]+=(k1[i]+2*k2[i]+2*k3[i]+k4[i])/6.0;
        return;
}
```